The Pennsylvania State University

The Graduate School

College of Engineering

MODELING THE EFFECTS OF FUEL ROD CRUD FORMATION ON BOILING HEAT TRANSFER IN A PRESSURIZED WATER REACTOR USING EULERIAN TWO-FLUID CFD

A Thesis in

Nuclear Engineering

by

Ashley Guzzetta

Submitted in Partial Fulfillment

of the Requirements

for the Degree of

Master of Science

May 2010

The thesis of Ashley Guzzetta was reviewed and approved* by the following:

Maria Avramova
Assistant Professor of Nuclear Engineering
Thesis Co-Advisor

Robert F. Kunz
Senior Research Associate, Applied Research Laboratory
Associate Professor of Aerospace Engineering
Thesis Co-Advisor

Kostadin Ivanov
Distinguished Professor of Nuclear Engineering
Thesis Reviewer

Jack S. Brenizer
J. 'Lee' Everett Professor of Mechanical and Nuclear Engineering
Chair of the Nuclear Engineering Department

*Signatures are on file in the Graduate School

ABSTRACT

This research focuses on Computational Fluid Dynamics (CFD) modeling of subcooled boiling in crudded nuclear reactor coolant passages. An Eulerian multiphase subcooled boiling model was implemented in a multidimensional CFD code to predict the heat transfer in vertical coolant passages with inlet subcooling, with and without crud deposits present on the heated surface. A subcooled nucleate boiling model based on partitioning of the relevant models of heat transfer is implemented. Specifically, models for sensible heating and quenching heating of the liquid, and heat and mass transfer modeling of evaporation and condensation are implemented in concert with the baseline interfacial dynamics models (i.e. drag, dispersion) in the code. This boiling model, adopted from the work of Podowski (1), is applicable to uncrudded/clean channel surfaces. The model was validated against two sets of experimental data and results compare favorably with the measurements.

In this thesis, a heat-apportionment based nucleate boiling model has been developed to model crudded systems. Crud conductivity, surface roughness, nucleation site density and frequency, bubble departure diameter, and crud porosity were accounted for, the latter in the context of modeling of wick boiling associated with the “chimney” structures that occur in crudded boiling. By comparing results of the crudded model to experimental data, it was observed that the model captures the essential heat transfer characteristics present in subcooled nucleate boiling of crudded systems.

TABLE OF CONTENTS

LIST OF FIGURES

LIST OF TABLES

NOMENCLATURE

Symbols

A_i'''	interfacial area density
A^{1f}, A^{2f}	fraction of area affected by heat flux
A^w	wick boiling area availability factor
α^k, α^l	volume fraction of fields k and l
α^l, α^v	volume fraction of liquid and vapor phases
C_p^l	specific heat of liquid phase
C_D , C_{TD}	drag coefficient, coefficient of turbulent dispersion
C_1 , C_2	k-ε model coefficients
C_μ	Prandtl-Kolmogorov constant
d^B	mean bubble departure diameter in bulk flow
d^{fl}	diameter of the flow area
d^w	bubble departure diameter at the wall
D, D^{kl}	drag force term, interfacial drag force term for fields k to l
D^{pore}	characteristic pore diameter
E	law-of-the-wall constant
ε	turbulent dissipation rate
ε^k, ε^l	turbulent dissipation rate of fields k and l
f	bubble departure frequency
g_i	gravity vector
Γ^{lk}, Γ^{kl}	mass transfer rate from field l to field k, and field k to field l
Γ^{lv}, Γ^{vl}	mass transfer rate from liquid to vapor, and vapor to liquid

h^k , h^l	enthalpy for fields k, l
h^f, h^g	enthalpy for saturated fluid and gas phases
h^l, h^v	enthalpy for liquid and vapor phases
h^{fg}, h^{fv}	$h^g - h^f$, $h^v - h^f$
h^{lf}, h^{lg}	$h^f - h^l$, $h^g - h^l$
H	heat transfer coefficient
$H^{l,S}$, $H^{l,Q}$	heat transfer coefficient for single phase convection, quenching
k	turbulence kinetic energy
k^k , k^l	turbulence kinetic energy of fields k and l
k^l	thermal conductivity of liquid phase
k^{crud}	thermal conductivity of crud
k	dimensional characteristic roughness height
k^+	surface roughness height
K	bubble influence factor
κ	Kolmogorov constant
M''	pore site area density
M_{i}^{lk}	non-drag forces for fields k to l
$\dot{m}$	mass transfer rate
μ, μ_t	molecular and eddy viscosity
N'''	nucleation site density
P^k	production of turbulent energy for field k
Pr_t	turbulent Prandtl number
$P_{\mathrm{r}\varepsilon}^k$, $P_{\mathrm{r}\varepsilon}^k$	turbulent Prandtl numbers for field k
p	pressure
q''	heat flux

$q''^{,net}$, $q''^{,w}$	net wall heat flux, wall heat flux
$q''^{,l,S}$, $q''^{,l,Q}$, $q''^{,v,E}$	heat flux for single phase convection, quenching, evaporation
Re^b	bubble Reynolds number
Re_D	Reynolds number
ρ^k, ρ^l	density of fields k and l
ρ^g, ρ^l	density of gas and liquid phases
ρ^g	density of vapor phase
$\vec{T}$	turbulent dispersion force
T^l, T^v	temperature of liquid and vapor phases
T^{int}, T^{sat}	temperature at the interface, saturation temperature
$T^{l,bulk}$	bulk liquid temperature
T^{sub}	degrees of subcooling
T^w	wall temperature
t^{crud}	crud thickness
t^w	bubble departure wait time
τ_{ij}^k	shear stress tensor for field k
τ_{ij}^l	shear stress tensor for liquid phase
τ_w	wall shear stress
U^+	U/U^*
u_j^k, u_i^l	Cartesian velocity component of field k and l
u_j^l, u_j^v	Cartesian velocity component for liquid and vapor phases
$\underline{V}^{rel}$	relative velocity
$\forall$	cell volume
v^*	friction velocity

x_j , x_i	Cartesian coordinates
$\langle x_e \rangle$	equilibrium quality
y^+	dimensionless wall distance

Superscripts, Subscripts

k , l	generic phase descriptor
f , g	saturated fluid and gas phase descriptor
l , v	liquid and vapor phase descriptor
i , j	Cartesian tensor indices
in, out	into and out of control volume

ACKNOWLEDGEMENTS

I would like to express my profound appreciation to a list of people who gave me support and help for the completion of this work.

I thank my research advisors Dr. Robert Kunz and Dr. Maria Avramova for the guidance in my research and accurate decisions concerning my academic requirements.

I thank Dr. Brenizer and Dr. Ivanov for spending time to read my thesis.

I also would like to express my gratitude to the faculty and staff of the Mechanical and Nuclear Engineering department as well as the Applied Research Laboratory in helping me reach my educational and research goals.

.

Chapter 1 Introduction

1.1 Background

In a pressurized water reactor (PWR), energy is produced in the fuel through fission resulting in heat generation. This heat is transferred to the outer surface of the fuel rod through conduction and is removed from the surface by convection to the reactor coolant. If either mechanism of heat transfer is reduced, fuel temperatures will increase which can ultimately cause fuel failure. It is possible for heat transfer to be reduced by crud formation on the fuel surface. When boiling is present, crud can give rise to either a decrease or increase in heat transfer as discussed in this chapter. Crud is the buildup of unwanted materials on fuel rod cladding in a light water reactor (LWR). Corrosion of steam generator tubes is the main source of crud deposits (2). Boron in the coolant can also be captured in the crud deposits. If a high concentration of boron species is present in the crud, axial offset anomaly (AOA) will result causing a crud induced power shift (CIPS).

In general, it is important to understand the heat transfer mechanisms inside the reactor in order to maintain fuel integrity. Accordingly, the heat transfer in a reactor with and without crud deposits should be studied to characterize the severity of heat transfer fluctuation due to crud buildup on fuel surfaces.

1.2 Boiling Mechanisms

A major design consideration in PWR's is to maintain the coolant at a specified pressure to prevent boiling within the reactor. The coolant enters the reactor a number of degrees below the saturation temperature, i.e., is subcooled. Boiling is prevented when the bulk temperature of the coolant and the surface of the fuel rod remain below the saturation temperature. Under these

conditions heat is primarily transferred to the coolant by single phase forced convection without causing a phase change as shown in Figure 1.1(a). If the temperature of the fuel surface exceeds saturation, localized boiling can occur on the surface of the fuel. Vapor bubbles nucleate on the wall at imperfections (known as nucleation sites), but most likely will not detach since the coolant is still subcooled. Instead, the bubbles collapse while still attached to the wall. For the infrequent case of bubble detachment, the bubbles will condense shortly after in the cold fluid. The net generation of vapor is negligible. This is referred to as subcooled nucleate boiling and is depicted in Figure 1.1(b). As the wall temperature increases, heat is added to the coolant and the bulk fluid temperature approaches saturation. Figure 1.1(c) shows that during this time the bubbles become larger and have a greater chance of detaching from the surface and entering the coolant stream. This is known as saturated boiling, or simply, nucleate boiling. When boiling occurs (for both subcooled and saturated conditions), heat transfer is enhanced because the motion of the bubbles enhances mixing in the fluid. Since heat transfer at the wall is enhanced, the wall temperature rises at a slower rate than in single phase convection (3). As the temperature of the fuel surface continues to increase, the density of the bubbles near the surface increases as well. Eventually, a bubble density is reached where the bubbles start to combine, or coalesce, leading to a vapor film on the fuel surface (Figure 1.1(d)). Vapor acts as a thermal insulator restricting heat removal from the surface. When this happens, convection is no longer the primary mechanism of heat removal. Heat now passes through the vapor into the coolant by conduction, a less efficient mechanism of heat transfer. Ultimately, this behavior leads to dryout conditions which can cause fuel failure.

Multiple boiling regimes have been discussed in this section. Single phase convection and nucleate boiling will be the focus of the research in this thesis.

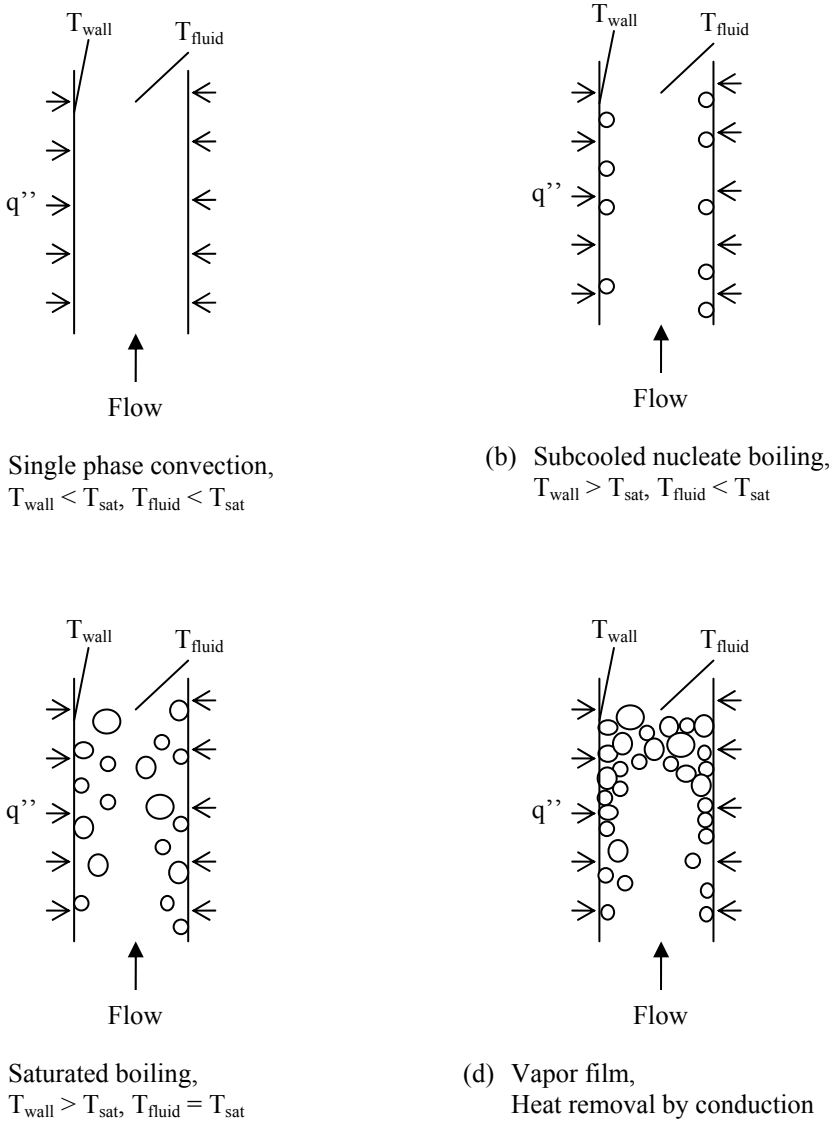

(a) Single phase convection, $T_{wall} < T_{sat}$, $T_{fluid} < T_{sat}$

(b) Subcooled nucleate boiling, $T_{wall} > T_{sat}$, $T_{fluid} < T_{sat}$

(c) Saturated boiling, $T_{wall} > T_{sat}$, $T_{fluid} = T_{sat}$

(d) Vapor film, Heat removal by conduction

Figure 1.1: Boiling Heat Transfer Regimes in a PWR Subchannel

1.3 **Crud Formation**

Under normal operating conditions, subcooled nucleate boiling occurs in the top grid span of some assemblies and is the primary mechanism for crud deposition. If thick enough, crud can cause heat transfer degradation or, in some circumstances, heat transfer enhancement, at the

fuel surface. (The latter is discussed further in Section 1.4.) Crud forms when bubbles detach from the surface of the cladding material during nucleate boiling. After detachment, the bulk fluid rushes underneath the bubble. When the cooler bulk fluid comes in contact with the significantly hotter fuel surface, some evaporation takes places leaving corrosion products and the boron present in the fluid to harden on the surface. This hardened deposit is known as crud. Figure 1.2 illustrates the deposition of crud on a fuel surface. Crud thickens as the bubble detachment and evaporation process is repeated multiple times. This thickening occurs over a long time period of normal operating conditions. The time scale of fluid flow is much less than the time scale of crud formation.

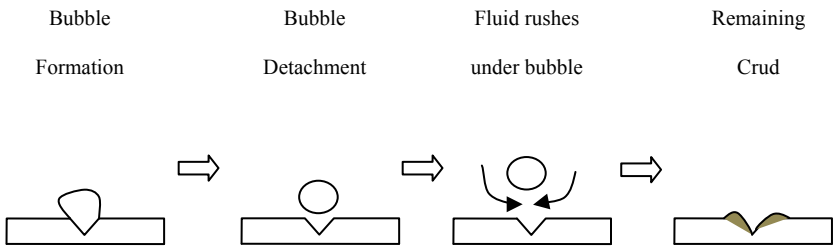

Figure 1.2: Process of Crud Deposition on Fuel Surface

1.4 **Characteristics of Crud**

Crud can possess a variety of properties and compositions, as well as different structural attributes depending on the circumstances of formation. These circumstances include operating conditions such as system pressure, coolant temperature, mass flow rate, and heat flux at the surface. Due to its fragile nature, crud deposits do not generally exceed a thickness of 1 mm (0.039 in) (4) because of its tendency to break away from the surface under operating conditions. As a result, most experimental measurements have been made on deposits created in a laboratory.

The composition of crud formed in a water cooled reactor is magnetite (5) with a chemical formula of Fe_3O_4. Structural properties of crud include porosity, density of chimneys, and size of chimneys. Also, thermal conductivity is an important property. Cohen (5) summarizes the thermal conductivity of crud with a range of structural properties as seen in Table 1.1. The conductivity ranges from 0.156 to 21.21 W/m-°K (0.09 to 14.0 Btu/hr-ft-°F) depending on porosity, chimney density, and chimney size, as well as heat transfer regime.

Table 1.1: Structure and Thermal Conductivity of Magnetite Deposits

Type and Description of Crud	Test Pressure/ Temperature	Max Heat Flux [Btu/hr-ft^2]	Heat Transfer Model	Min Thickness [mil]	Max Thickness [mil]	Effective Conductance, k [Btu/hr-ft-°F]
Isotropic Porous, 70-90% voids	70 bar (1015 psi)	159,000	Boiling	0.14 (3.56 µm)	2.68 (68.07 µm)	0.09 to 0.75
Isotropic porous, 60-70% voids with 5µ chimneys 5000/sq	69 bar (1001 psi)	844,000	Boiling	1.18 (29.97 µm)	3.94 (100.08 µm)	2.0 to 3.0
Isotropic, low porosity, compact	554 °F	919,000	Nonboiling	0.85 (21.59 µm)	1.7 (43.18 µm)	3
			Subcooled Boiling			
Isotropic, low porosity with 10µ chimneys 5000/sq	554 °F	770,000 to 919,000	Nonboiling			173 to 1.90
			Subcooled Boiling			10.6 to 14.0

1.5 **Heat Transfer on Crudded Surfaces**

Cohen and Taylor (6) documented the effects of porous deposits of magnetite on forced convection heat transfer in subcooled nucleate boiling. Results of subcooling temperatures between clean and crudded surfaces at varying heat fluxes were compared and are shown in Figure 1.3. In the single phase regions, $\Delta T^{crud} > \Delta T^{clean}$ due to an insulation effect of the crud. On the test section with crud deposits, transition from single-phase forced convection to nucleate boiling is approximately 10 °K (22 °F) lower than for the clean surface with half of the heat flux applied. For both clean and crudded surfaces, the heat transfer coefficient increases due

to boiling, therefore, the slope increases once the two-phase region is entered. The slope of the crudded two-phase line is somewhat steeper than the clean two-phase line. Indeed, when the heat flux exceeds approximately 1200 kW/m^2 (390,000 Btu/hr-ft^2), the fouled surface has less superheat (lower wall temperature). This increase in slope is associated with observations made during the boiling process where the crudded surface had a large number of nucleation sites with a small bubble departure diameter. On the other hand, the clean surface had a smaller number of nucleation sites with a larger bubble departure diameter. Also, as discussed in detail next, wick boiling can arise on crudded surfaces. Together, these physics can give rise to higher heat transfer coefficients compared to clean surfaces at high heat fluxes augmenting heat transfer in two-phase conditions.

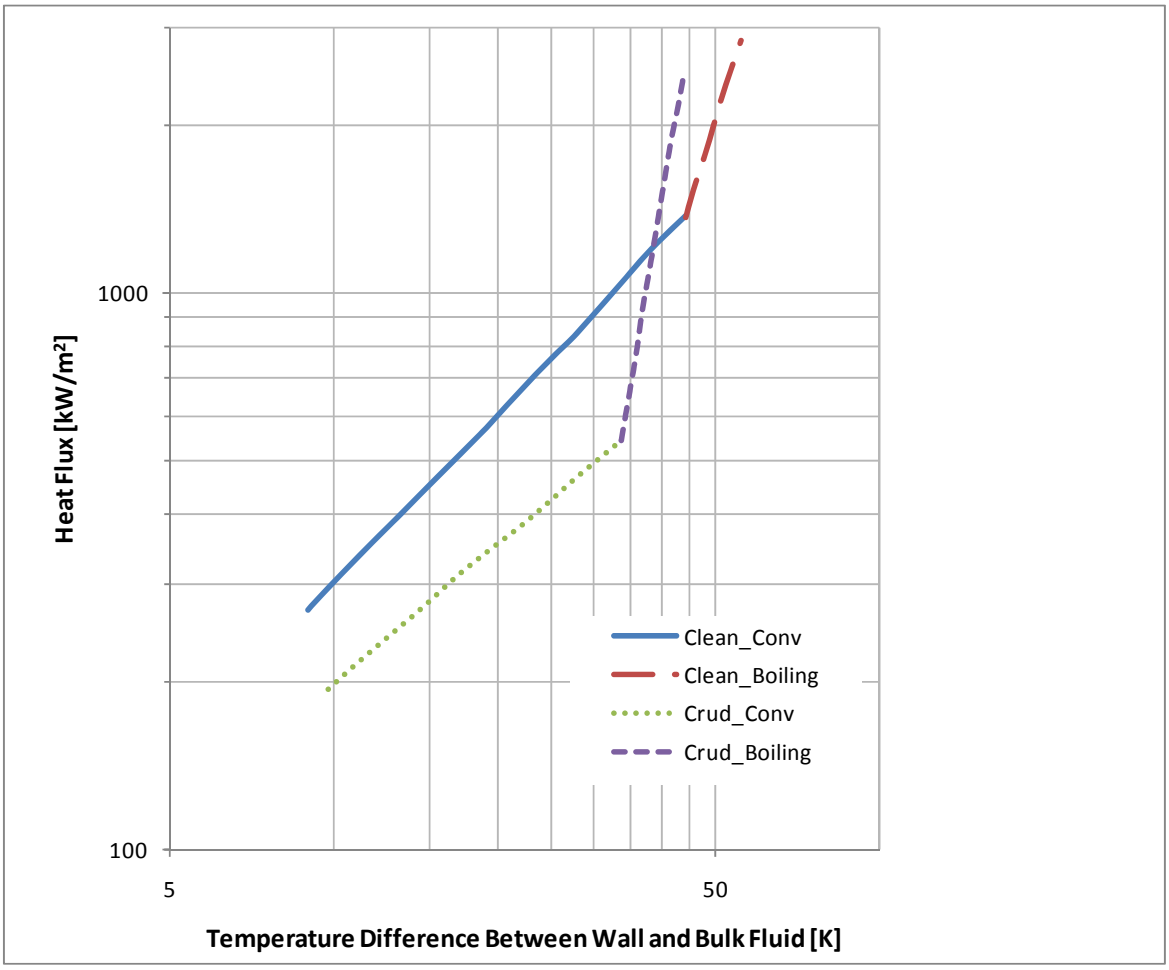

Figure 1.3: Temperatures on Clean and Fouled Surfaces with Varying Heat Flux

The thickness of the deposits influences heat transfer conditions drastically. This can be seen in Figure 1.4 **(5)** where the heat flux is plotted versus wall temperature elevation due to crud for different crud thicknesses. The plot is created from data in an experiment on heat transfer in bulk boiling **(4)**. In this experiment, the inside wall temperature of a heater rod was measured when the outer surface was clean and again when crud deposits were present. Since the two temperatures were measured at the same position on the test section and the same operating conditions, the difference between them represents the elevation in outer rod surface temperature caused by the crud deposit. The figure shows that the thicker the crud deposits are, the more the wall temperature is increased at a certain heat flux. Also shown is a specimen impregnated with hardening compounds to produce nonporous crud. There is a large increase in wall temperature for this specimen showing heat transfer is considerably poorer in nonporous crud. This could be due to the inability of wick boiling to take place.

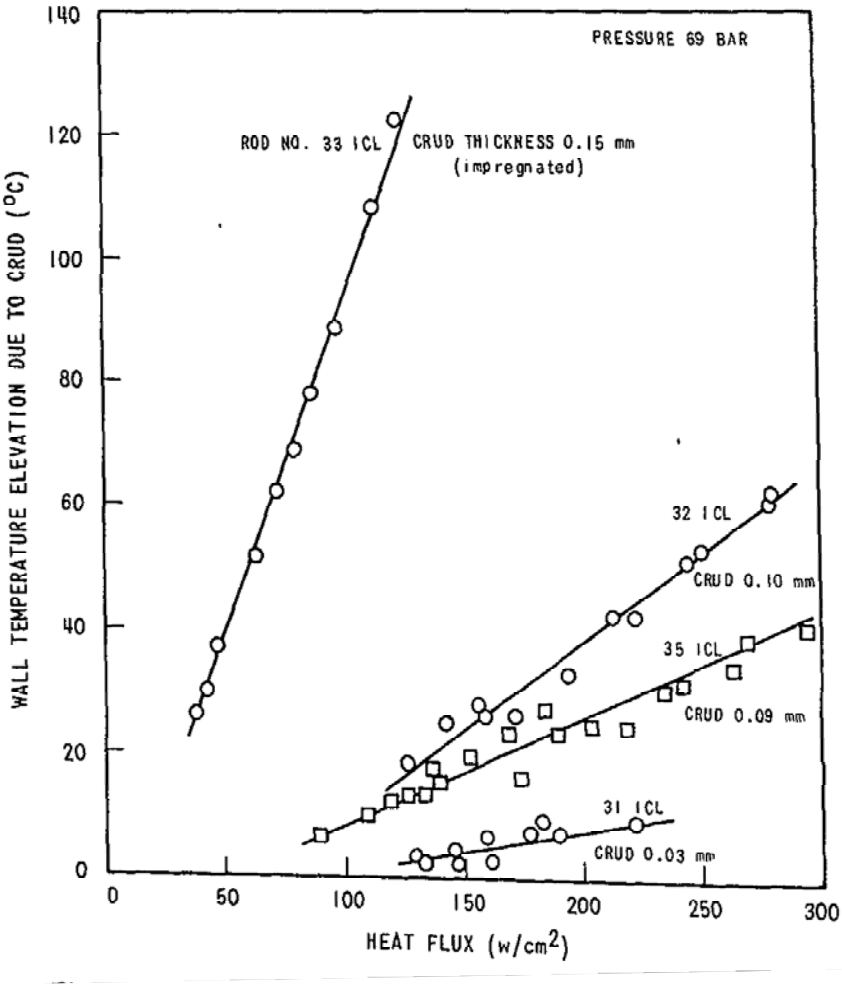

Figure 1.4: Wall Temperature Elevation due to Crud

When crud is porous, so called "chimneys" form as a means of heat removal through the deposit. This process of boiling heat transfer on a heated surface overlaid by porous crud is known as wick boiling. It is discussed by Pan (7) and is illustrated in Figure 1.5. Through capillary action, it is assumed that coolant is drawn into the crud through smaller pores to the evaporative surface by surface tension. The resulting vapor is then ejected via larger diameter pores known as chimneys. As the heat flux increases and/or the crud thickens, all the liquid drawn into the porous crud vaporizes potentially causing safety concerns such as dryout. When

crud composed of porous magnetite becomes impregnated with components other than iron, wick boiling becomes severely restricted resulting in excessive temperature elevation rise at the fuel surface.

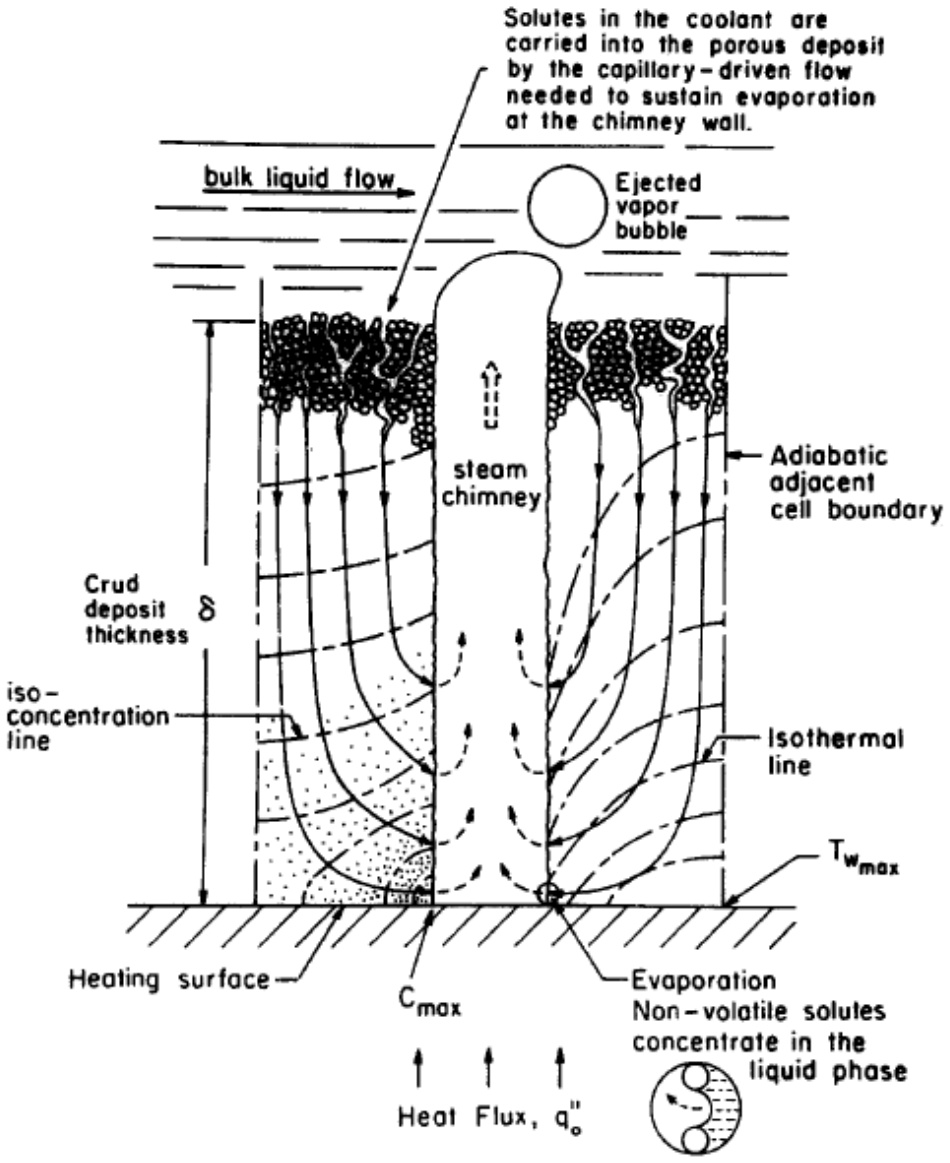

Figure 1.5: Wick Boiling Model

1.6 Literature Review

1.6.1 Two-Phase Heat Transfer Modeling

Modeling of two-phase heat transfer can be very complex, but it is necessary to perform multi-phase heat transfer analysis to understand the boiling behavior in a heated channel. The most conventional two-phase heat transfer model used in CFD is the Eulerian two-phase approach. In this model, there are phase-specific continuity equations used to solve phase distributions with a separate set of momentum equations solved for each term. In two-phase bubbly flow with heat transfer, an energy equation is solved for both the liquid and vapor phases. Exchange of mass, momentum, and energy between phases are modeled using the source terms present in the balance equations. Multiple two-fluid heat transfer models were studied and are summarized in this section.

Kurul and Podowski (8) developed a two-dimensional, two-fluid, time-averaged approach while combining phase-change and interfacial momentum and energy transport in both the axial and lateral directions. The lateral transport of vapor between the heated wall and subcooled liquid is based on thermodynamic equilibrium phenomena discussed and modeled. The parameters used in this 2-D model were validated against 1-D drift flux calculations. The total heat flux was split into three parts: single-phase convection, quenching, and evaporation. With each heat transfer component, a heat transfer coefficient is determined analytically to calculate the percentage of heat transfer consumed for that component.

Mathematical modeling concepts used to develop multidimensional models of forced convection boiling are presented by Podowski et al. (1). In this model, a complete mechanistic multidimensional model of two phase flow was coupled with the governing equations for heat transfer and phase change in heated channels. The model includes conservation equations for each field, a turbulence model, interfacial mass transfer, interfacial momentum transfer,

interfacial energy transfer, thermal boundary conditions of near-wall heat transfer, and kinematic boundary conditions for phasic velocities.

Krepper (9) assessed two-fluid heat transfer models for internal bubbly flow with wall boiling. His model was based on the main context of Kurul and Podowski (8). The total heat flux is partitioned into three parts: single phase turbulent convection, quenching, and evaporation. The turbulent convection heat flux uses a correlation developed by Egorov and Menter (10) multiplied by the area fraction of single phase. The quenching heat flux correlation used is similar to the model by Kurul and Podowski where it is represented in terms of the quenching heat transfer coefficient. The temperature at the near wall cell was defined by the characteristic temperature to obtain a grid independent solution. The characteristic temperature is given by the non-dimensional turbulent boundary layer profile of the temperature, T^+, and a constant non-dimensional distance, y^+, is defined. In the model, the evaporation heat transfer is obtained using a model that accounts for evaporative mass flux on the wall. Correlations for nucleation site density, bubble diameter, waiting time, bubble frequencgy, bubble influence factor, and quenching heat transfer coefficient are taken from Kurul and Podowski. A bubble departure diameter is used from Tolubinsky and Kostanchuk (11) that is case dependent on liquid subcooling.

Bae (12) uses the same approach to Krepper in developing a subcooled boiling model. The only notable difference is that Bae chooses to use half the value of bubble influence factor than used by Krepper. Bae also parameterized a number of the component models.

A model for subcooled nucleate boiling flow in a vertical channel was developed by Kljenek (13). The model couples a three-dimensional bubble-tracking model with a two-dimensional two-fluid model. In the bubble-tracking model, the dynamic and thermal behavior of each bubble in the liquid are simulated individually. The overall behavior of the system composed of liquid and vapor results from bubble motion, interaction, coalescense, and boiling mechanisms. In this approach, the modeling of the liquid flow field, including the liquid

turbulence that affects bubble interaction, is difficult. In the two-fluid model, both the liquid and vapor phases use their own system of averaged equations for mass, momentum, and energy. The averaged equations are coupled with closure relations to incorporate the exchange of mass, momentum, and energy at the interface. The two-fluid model does not account for varying bubble size. Because of this, bubble size is accounted for in an extra model or by using closure relations.

A two-phase wall heat transfer model for subcooled boiling flow is described by Steiner (14). He specifically uses a superposition model where the total heat flux is composed of only two components: forced convection and nucleate boiling. It is based on a model by Chen (15) that was originally developed for saturated boiling flow. A suppression factor was used to bridge the region between pure single-phase convection and fully developed nucleate boiling. The suppression factor was based on bulk flow Reynold's number as the only correlation parameter. Doing this makes the model based on a single-phase bulk flow quantity and hard to quantify in complex flow geometries. These two drawbacks allow for Steiner to improve on Chen's model using a boiling departure lift-off model. Steiner's model uses a suppression factor dependent on local flow quantities. The models of Steiner and Chen were coupled to overcome their shortcomings.

1.6.2 Experimental Results

Experimental studies of boiling are ubiquitous in nuclear engineering and other literature. In this thesis, the focus is on local conditions based nucleate boiling modeling. Therefore, we consider two experimental data sets that in concert contribute to this effort by providing: 1) physics understanding, and 2) local conditions validation data in the context of clean and crudded nucleate boiling.

A classic experimental study of subcooled boiling on clean surfaces was performed by many. Of specific interest was an experiment done by Bartolomej (16; 17). He performed subcooled boiling experiments in which upward water flow in a heated tube was subjected to high pressures between 7 and 15 MPa (1015 and 2176 psi). The upper end of these pressures are comparable to the operating pressures in PWR's. A uniform mass flux of 900 kg/m^2-s was used and the inlet subcooling varied from 293.15 to 433.15 °K (68 to 320 °F). Heat flux was studied between 400-800 kW/m^2. A two meter long vertical tube was used for testing with an inner diameter of 15.44 mm (0.61 in). The vapor volume fraction results were recorded in the subcooled boiling region along with temperature profiles and outer wall temperatures. The influence of heat flux, mass flow rate, pressure, and liquid subcooling on the vapor volume fraction was studied. In the results, the vapor volume fraction at the exit varied from 0 to 0.5. As expected, it was concluded that void fraction decreases at a specific axial location when mass flux increases and also when heat flux decreases.

Cohen and Taylor (6) contributed experimental data showing the effects of porous deposits of magnetite on forced convection heat transfer in subcooled nucleate boiling. This is one of the only available published set of data on the performance of boiling crudded heat exchangers. Results of subcooled temperatures between clean and crudded surfaces at varying heat fluxes were compared. The saturated temperature of the test was $T^{sat} \sim 394.3$ °K (250 °F) (6) corresponding to $P^{sat} = 0.2057$ MPa (29.8 psi). It is clear that this pressure is much lower than the operating pressure of a typical PWR (~15.5 MPa/ 2250 psi). The test included a hollow cylinder heated electrically with an internal thermocouple placed on the metallic surface of the specimen. The porous deposit that formed from precipitated deposits was 25.4 μm thick (1 mil) with a thermal conductivity, k, of 0.864 W/m-°K (0.5 Btu/hr-ft-°F). Cohen reported linear regression fits of this test that can be seen in Figure 1.3. Experimental observations were made during the boiling process such that the crudded surface had a large number of nucleation sites with a small

bubble departure diameter. On the other hand, it was observed that the clean surface had a smaller number of nucleation sites with a larger bubble departure diameter. This effect can contribute to the enhanced heat transfer of the crudded surface in the two-phase region.

1.7 **Research Objectives**

The objective of this research is to implement Eulerian multiphase subcooled boiling models in a multidimensional CFD code, to validate the model, and to extend its applicability to crudded conditions.

The starting point for the research is an Eulerian two-fluid CFD model. This is used as a framework of implementation of a subcooled nucleate boiling model based on partitioning of the relevant models of heat transfer in these systems. Specifically, models for sensible heating and quenching heating of the liquid, and heat and mass transfer modeling of evaporation and condensation are implemented in concert with the baseline interfacial dynamics models (i.e. drag, dispersion). This boiling model, adapted from the work of Podowski (1), is applicable to uncrudded/clean channel surfaces.

Extension of the heat-apportionment based nucleate boiling model to crudded systems involves the development of several physics models. Dimensional analysis and qualitative experimental observations were used to do this. In this thesis, the crudded boiling model is developed and calibrated against available, bulk experimental data available in literature.

The model captures the essential heat transfer physics in these systems, by accounting for crud conductivity, surface roughness, enhanced nucleation site density and rate, reduced bubble departure diameter and, importantly, wick boiling.

The thesis is organized as follows: In Chapter 2, the theoretical formulation pertaining to the two-fluid Navier Stokes equations, two-phase heat transfer model, and crud modeling is presented. Then, the numerics of the CFD method are reviewed. In Chapter 3, experimental

results are used to validate the heat transfer model developed for boiling on a clean surface. In Chapter 4, the crudded boiling model is assessed using data from Cohen and Taylor (6). Chapter 5 provides conclusions and a discussion of recommended future work.

Chapter 2 Theoretical Formulation

The following sections present the governing equations, physical modeling, and numerical methods used in this research.

2.1 Governing Equations

The ensemble averaged single-pressure two-fluid differential system employed cast in Cartesian coordinates is presented in Equations 2.1-2.6.

Conservation of mass:

$$\frac{\partial}{\partial \mathrm{t}}\left(\alpha^k \rho^k\right) + \frac{\partial}{\partial \mathrm{x_j}}\left(\alpha^k \rho^k \mathrm{u_j^k}\right) = \sum_{k \neq l} \left(\Gamma^{lk} - \Gamma^{kl}\right) \tag{2.1}$$

Conservation of momentum:

$$\begin{aligned} &\frac{\partial}{\partial \mathrm{t}}\left(\alpha^k \rho^k \mathrm{u_i^k}\right) + \frac{\partial}{\partial \mathrm{x_j}}\left(\alpha^k \rho^k \mathrm{u_j^k u_i^k}\right) \\ &\qquad = -\alpha^k \frac{\partial \rho}{\partial \mathrm{x_i}} + \alpha^k \rho^k \mathrm{g_i} + \frac{\partial \tau_{ij}^k}{\partial \mathrm{x_j}} + M_\mathrm{i}^{lk} + \sum_{k \neq l} \left(D^{kl}\left(\mathrm{u_i^l} - \mathrm{u_i^k}\right) + \Gamma^{lk}\mathrm{u_i^l}\right. \\ &\qquad \left. - \Gamma^{kl}\mathrm{u_i^k}\right) \end{aligned} \tag{2.2}$$

Conservation of energy:

$$\frac{\partial}{\partial \mathrm{t}}\left(\alpha^k \rho^k \mathrm{h}^k\right) + \frac{\partial}{\partial \mathrm{x_j}}\left(\alpha^k \rho^k \mathrm{u_j}^k \mathrm{h}^k\right) = \tau_{ij}^k \frac{\partial \mathrm{u_i}^k}{\partial \mathrm{x_j}} + \alpha^k \mathrm{u_j}^k \frac{\partial p}{\partial \mathrm{x_j}} + q''_{net} + Mass\ Transfer\ Terms \quad \textbf{2.3}$$

where the stress tensor term, τ_{ij}^k is written:

$$\tau_{ij}^k = \alpha^k \mu_{\mathrm{t}}^k \left[\frac{\partial \mathrm{u_i}^k}{\partial \mathrm{x_j}} + \frac{\partial \mathrm{u_j}^k}{\partial \mathrm{x_i}}\right] \quad \textbf{2.4}$$

Here, superscript *k* is the species or "field" designator. In this work, each field's density is taken as constant. Interfacial drag and non-drag forces, D^{kl} and M_{i}^{lk}, respectively, appear in the momentum equation. Inter-field mass transfer rates, Γ^{lk} are incorporated. In the force and mass transfer terms, superscripts *k* and *l* represent donor and receptor fields. Net wall heating, q''_{net}, and mass transfer terms appearing in Equation 2.3 arise in the boiling model formulation presented below.

The eddy viscosity,μ_t, is provided through a multiphase extension to the high-Reynolds number k-ε turbulence model.

Conservation of turbulence kinetic energy, k:

$$\frac{\partial}{\partial \mathrm{t}}\left(\alpha^k \rho^k \mathrm{k}^k\right) + \frac{\partial}{\partial \mathrm{x_j}}\left(\alpha^k \rho^k \mathrm{u_j}^k \mathrm{k}^k\right) = \frac{\partial}{\partial \mathrm{x_j}}\left(\alpha^k \frac{\mu_{\mathrm{t}}^k}{P_{\mathrm{rk}}^k} \frac{\partial \mathrm{k}^k}{\partial \mathrm{x_j}}\right) + P^k - \alpha^k \rho^k \varepsilon^k \quad \textbf{2.5}$$

Conservation of turbulence energy dissipation rate, ε:

$$\frac{\partial}{\partial \mathrm{t}}\left(\alpha^k \rho^k \varepsilon^k\right) + \frac{\partial}{\partial \mathrm{x_j}}\left(\alpha^k \rho^k \mathrm{u_j^k} \varepsilon^k\right) = \frac{\partial}{\partial \mathrm{x_j}}\left(\alpha^k \frac{\mu_\mathrm{t}^k}{P_{\mathrm{r}\varepsilon}^k} \frac{\partial \varepsilon^k}{\partial \mathrm{x_j}}\right) + C_1 \frac{\varepsilon^k}{\mathrm{k}^k} P^k + \left(-C_2 \frac{\varepsilon^k}{\mathrm{k}^k} \alpha^k \rho^k \varepsilon^k\right) \quad \textbf{2.6}$$

In this model, the eddy viscosity, μ_t, is computed from the Prandtl-Kolmogorv relation:

$$\mu_t = \frac{\rho C_\mu \mathrm{k}^2}{\varepsilon} \quad \textbf{2.7}$$

For the dispersed bubbly flows considered, the k-ε model is employed for the liquid phase only. In this thesis, only statistically steady-state boiling is considered. This means the time derivative terms in Equations 2.1 through 2.6 are neglected.

2.2 **Multiphase Modeling**

2.2.1 Interfacial Dynamics

In bubbly flow systems, it is necessary to incorporate models for the forces at the interfaces which are averaged away in the context of Eulerian two-fluid modeling. For low vapor fraction systems as considered in this research, typically, force models are adopted for drag, turbulence dispersion, bubble lift, and "wall repulsion". In the present work, a conventional bubble drag model is employed ((18), for example):

$$D = \frac{1}{8}\rho^l C_D \left|\underline{V}^{rel}\right| \underline{V}^{rel} A_i''' \quad \textbf{2.8}$$

This drag model is used for spherical bubbles where the interfacial area density, A_i''', and drag coefficient, C_D, are expressed as:

$$A_i''' = \frac{6\alpha^v}{d^B} \quad \textbf{2.9}$$

$$C_D = \frac{24}{Re^b} \quad \textbf{2.10}$$

$$Re^b = \frac{\rho^l |\underline{V}_{rel}| d^B}{\mu^l} \quad \textbf{2.11}$$

where d^B is the local bubble diameter and Re^b is the bubble Reynolds number.

A turbulence dispersion model developed by DeBartadano (19) is employed:

$$\vec{T} = C_{TD}\rho^l k^l D\alpha^l \quad \textbf{2.12}$$

where k^l is the liquid turbulence kinetic energy and the coefficient of turbulent dispersion, $C_{TD} = 1$.

Drag and dispersion forces are included to capture the first order dynamics effects of slip velocity and cross-channel vapor dispersion.

Many researchers also include interfacial dynamics models for lift and wall repulsion forces. Although such models are widely used, their formulation and physical consistency varies considerably. Indeed several researchers have shown that lift coefficients in standard lift models vary in magnitude and even switch signs depending on system conditions (20). Also, the physics of "wall forces" have been ascribed to lubrication (21) and wall repulsion (22), (both unlikely players in boiling flows), and kinematic constraints based on wall impermeability for a given bubble diameter. (The latter is not applicable to boiling flows where a wide range of bubble diameters are present at the heated walls.)

Accordingly, in this work, both lift and wall repulsion are not modeled. Bae (12) shows some second order effects of these models on subcooled boiling model predictions, but for this research, it is felt that these models are physically inappropriate in subcooled boiling systems. Development of more appropriate lift and repulsion models are identified as future work.

2.2.2 Heat and Mass Transfer Modeling

In subcooled nucleate boiling, there are three possible interfacial heat transfer mechanisms that can arise. These are liquid superheat induced evaporation (boiling), liquid subcooling induced condensation, and vapor superheat induced evaporation. In the present work it is assumed that the vapor remains at saturation and only liquid subcooling and or superheating drive interfacial heat and mass transfer. The first mechanism considered is boiling, i.e., liquid superheat induced evaporation. The situation is depicted in Figure 2.1 where an infinitely thin stationary control volume, ∀, contains the moving liquid-vapor interface.

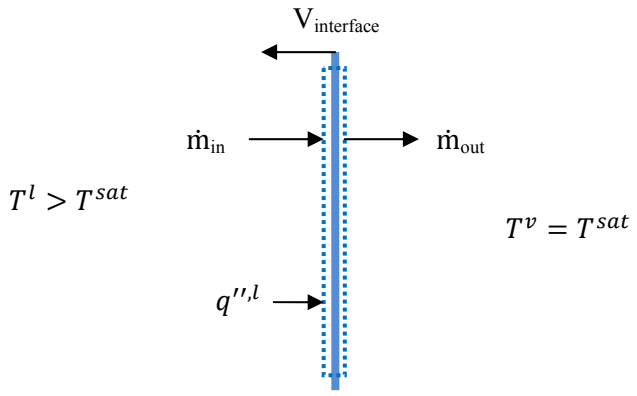

Figure 2.1: Liquid Superheat Induced Evaporation

The interfacial heat flux is defined by:

$$q'' = H(T^l - T^{int}) \quad \textbf{2.13}$$

Assuming that the interace is at saturation, Equation 2.13 becomes:

$$q'' = H(T^l - T^{sat}) \quad \textbf{2.14}$$

The heat flux is positive here since $T^l > T^{sat}$ and flows from the liquid to the interface resulting in evaporation.

Applying conservation of mass and energy yields Equations 2.15 and 2.16. In Equation 2.16, mass is donated at the liquid enthalpy and the receptor vapor enthalpy is at saturation.

$$\dot{m}_{in} = \dot{m}_{out} \quad \textbf{2.15}$$

$$\dot{m}_{out}h^g - \dot{m}_{in}h^l = q''^{,l} \quad \textbf{2.16}$$

Next, considering the interface instantaneously leaving the stationary control volume in Figure 2.2 and applying conservation of mass we arrive at Equation 2.17.

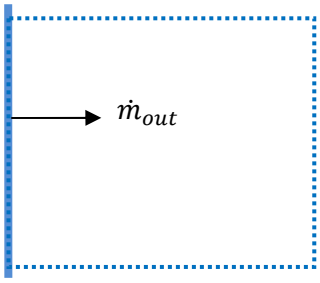

Figure 2.2: Stationary Control Volume where Interface is Entering

$$\dot{m}_{out} = \Gamma^{lv} \quad \textbf{2.17}$$

Combining Equations 2.15 and 2.17 results in Equation 2.18.

$$\dot{m}_{out} = \dot{m}_{in} = \Gamma^{lv} \quad \textbf{2.18}$$

Combining Equations 2.16 and 2.18 results in Equation 2.19, which simplifies to Equation 2.20.

$$\Gamma^{lv} h^g - \Gamma^{lv} h^l = q''^{,l} \quad \textbf{2.19}$$

$$q''^{,l} = \Gamma^{lv} h^{lg} \quad \textbf{2.20}$$

Conservation of energy can be derived using a simple two-fluid finite volume with only evaporation present. Consider saturated vapor and superheated liquid entering a control volume as depicted in Figure 2.3.

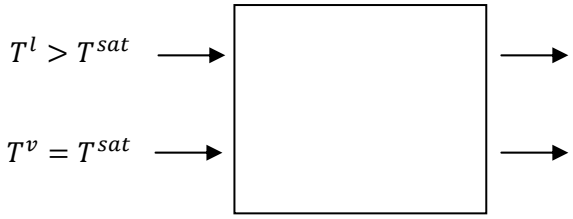

Figure 2.3: Two-Fluid Finite Volume Example for Evaporation

Conservation of energy for vapor and liquid can be written:

$$\dot{m}^v_{out} h^v_{out} - \dot{m}^v_{in} h^v_{in} = \Gamma^{lv} h^g \quad \textbf{2.21}$$

$$\dot{m}_{out}^{l} h_{out}^{l} - \dot{m}_{in}^{l} h_{in}^{l} = -q''^{,l} - \Gamma^{lv} h^{l} \quad \textbf{2.22}$$

Equation 2.21 can be manipulated to become:

$$\dot{m}_{out}^{l} h_{out}^{l} - \dot{m}_{in}^{l} h_{in}^{l} = -\Gamma^{lv} \mathrm{h}^{l} - \Gamma^{lv} (\mathrm{h}^{fg} + \mathrm{h}^{lf}) \quad \textbf{2.23}$$

The form of the energy equation shown in Equation 2.23 illustrates that the interfacial heat and mass transfer can be viewed as consisting of the enthalpy exchanged between phases by mass transfer, the enthalpy required to cool the liquid to saturation, and the enthalpy of formation of the vapor.

The other important interfacial heat transfer mechanism is subcooled boiling systems is liquid subcooling induced condensation indicated schematically in Figure 2.4. Since $T^{l} < T^{sat}$ for this situation, the interfacial heat flux, $q''^{,l}$, is negative, i.e., heat flows from the interface to the liquid and condensation is induced by cooling of the interface.

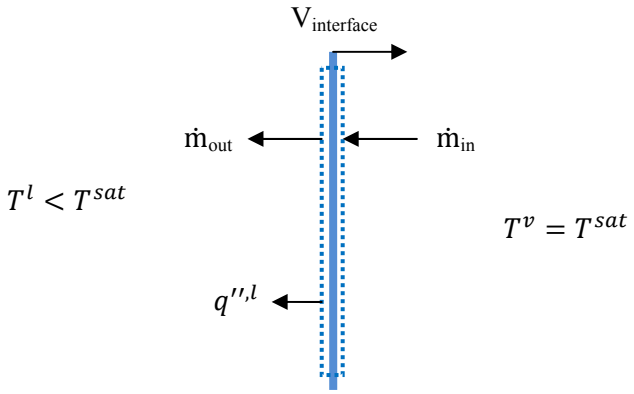

Figure 2.4: Liquid Subcooling Induced Condensation

Using the same approach presented for evaporation, conservation of mass and energy are applied.

$$\dot{m}_{in} = \dot{m}_{out} \quad \textbf{2.24}$$

$$\dot{m}_{out} h^f - \dot{m}_{in} h^v = -q''^{,l} \quad \textbf{2.25}$$

$$q''^{,l} = \Gamma^{vl} h^{fv} \quad \textbf{2.26}$$

Again, mass is donated at the local donor enthalpy (h^v) and arrives at saturation (h^f).

Consider subcooled liquid entering a control volume depicted in Figure 2.5.

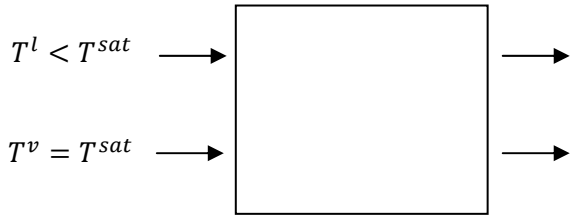

Figure 2.5: Two-Fluid Finite Volume Example for Condensation

The energy equations for vapor and liquid of this system are:

$$\dot{m}^v_{out} h^v_{out} - \dot{m}^v_{in} h^v_{in} = -\Gamma^{vl} h^v \quad \textbf{2.27}$$

$$\dot{m}^l_{out} h^l_{out} - \dot{m}^l_{in} h^l_{in} = q''^{,l} + \Gamma^{vl} h^f = \Gamma^{vl} h^v \quad \textbf{2.28}$$

Combining evaporation and condensation mass and heat transfer, the complete conservation equations for mass and energy employed here are:

$$\frac{\partial}{\partial \mathrm{x_j}} \left(\alpha^l \rho^l \mathrm{u}^l_\mathrm{j} \right) = \Gamma^{vl} - \Gamma^{lv} \quad \textbf{2.29}$$

$$\frac{\partial}{\partial x_j}\left(\alpha^v \rho^v u_j^v\right) = \Gamma^{lv} - \Gamma^{vl} \quad \textbf{2.30}$$

$$\frac{\partial}{\partial x_j}\left(\alpha^l \rho^l u_j^l h^l\right) = \tau_{ij}^l \frac{\partial u_i^l}{\partial x_j} + \alpha^l u_j^l \frac{\partial p}{\partial x_j} - q''^{,l} - \Gamma^{lv} h^l + \Gamma^{vl} h^v \quad \textbf{2.31}$$

$$\frac{\partial}{\partial x_j}\left(\alpha^v \rho^v u_j^v h^v\right) = \tau_{ij}^v \frac{\partial u_i^v}{\partial x_j} + \alpha^v u_j^v \frac{\partial p}{\partial x_j} + \Gamma^{lv} h^l + \Gamma^{lv}(h^{fg} + h^{lf}) - \Gamma^{vl} h^v \quad \textbf{2.32}$$

Note that the form of the energy equation present in the above equations does not include direct heating to the liquid or vapor from the wall. This subject is considered in the next section.

2.2.3 Heat Apportionment

For nucleate boiling, part of the heat flux from the wall is expended in bubble generation (boiling) and the rest is transferred to the liquid. The amount of vapor generation can be found by apportioning the wall heat flux into separate heat transfer components. Following Podowski et al. (1), (8), the total heat flux from the wall can be partitioned into three components: single phase convection, $q''^{,l,S}$, evaporation (heat that goes directly into generating vapor), $q''^{,v,E}$, and quenching heat flux (heat transferred to the liquid), $q''^{,l,Q}$.

$$q''^{,w} = q''^{,l,S} + q''^{,v,E} + q''^{,l,Q} \quad \textbf{2.33}$$

Equation 2.33 can be written as:

$$\begin{aligned} q''^{,w} &= q''^{,l,S} + q''^{,v,E} + q''^{,l,Q} \\ &= H^{l,S}\left(T^w - T^{l,bulk}\right) + H^{l,Q}\left(T^w - T^{l,bulk}\right) + q''_{v,E} \end{aligned} \quad \textbf{2.34}$$

The fraction of wall heat transferred to the liquid either by single phase convection or quenching is defined as:

$$q''^{,l,S} + q''^{,l,Q} = q''^{,w} - q''^{,v,E} \quad \textbf{2.35}$$

In this form, $q''^{,v,E}$ is identified as the liquid superheat induced evaporation heat flux, $q''^{,l}$, from Section 2.2.2. Specifically, a portion of the total wall heat flux is treated as going directly into evaporation.

For clean heat transfer surfaces, the following heat transfer models are adapted (Schlichting, (23)):

$$q''^{,l,S} = \left[\frac{C_\mu^{\frac{1}{4}}\rho^l(\mathrm{k}^l)^2}{\frac{1}{\kappa}\ln(Ey^+)}Pr_tC_p^l\right]A^{1f}(T^w - T^l) \quad \textbf{2.36}$$

$$q''_{v,E} = N'''f\left(\frac{\pi}{6}(d^B)^3\right)\rho^g h^{fg} \quad \textbf{2.37}$$

$$q''^{,l,Q} = \left(\frac{2}{\sqrt{\pi}}\sqrt{t^w\mathrm{k}^l\rho^lC_p^lf}\right)A^{2f}(T^w - T^l) \quad \textbf{2.38}$$

where f is the bubble departure frequency, T^w is the temperature of the heated wall, T^l is the bulk temperature of the subcooled liquid (here taken as the liquid temperature at the center of the wall adjacent cell), A^{1f} and A^{2f} are the area fractions, N''' is the nucleation site density, and d^B is the mean bubble diameter. Standard turbulence model parameters, $C_\mu = 0.09$, $\kappa = 0.4187$, $E = 9.793$, and $Pr_t = 0.91$ are specified per the wall-function based high Reynolds number $k-\varepsilon$ model used. The thermal conductivity, density, and specific heat of the liquid phase are represented by k^l, ρ^l, and C_p^l, respectively. The density of the vapor phase is ρ^g and t^w is the waiting time between the bubble departure and the appearance of the next bubble at the same nucleation site.

The area fractions, A^{1f} and A^{2f}, are the fraction of area affected by the sensible and quenching heat flux components defined as (12):

$$A^{1f} = \max\left(1 - A^{2f}, 0\right) \quad \textbf{2.39}$$

$$A^{2f} = N''' \frac{\pi (d^B)^2}{4} \cdot \mathrm{K} \quad \textbf{2.40}$$

In Equation 2.40, K is the bubble influence factor defined as the ratio of the area influenced by nucleate boiling to the projected area at the bubble departure. In this work, K=1.

Nucleation site density is the number of active (boiling) nucleation sites per unit area determined by (1):

$$N''' = [185(T^w - T^l)]^{1.805} \quad \textbf{2.41}$$

where ΔT is in °C and N''' is in $^1/_{m^2}$.

The bubble departure diameter is determined from (9):

$$d^B = \min\left(0.0006 \cdot exp\left(\frac{-\Delta T_{sub}}{45}\right), 0.0014\right) \quad \textbf{2.42}$$

where ΔT_{sub} is in °C and d^B is in m.

The bubble departure frequency is calculated as (9):

$$f = \sqrt{\frac{4g(\rho^l - \rho^l)}{3d^B\rho^l}} \quad \textbf{2.43}$$

Here, the waiting time is taken as 80% of the bubble departure period (8):

$$t^w = \frac{0.8}{f} \quad \textbf{2.44}$$

The heat apportionment algorithm is implemented as follows: For a given net wall heat flux, the evaporative heat flux, $q''^{,v,E}$, is computed from Equation 2.37 for each heated wall face. The remainder of the flux must be partitioned between $q''^{,l,S}$ and $q''^{,l,Q}$ as follows:

$$q''^{,w} - q''^{,v,E} = H^{l,S}\left(T^w - T^{l,bulk}\right) + H^{l,Q}\left(T^w - T^{l,bulk}\right) \quad \textbf{2.45}$$

with heat transfer coefficients for single phase convection (24) and quenching (9) defined as:

$$H^{l,S} = \frac{C_\mu^{\frac{1}{4}}\rho^l(\mathrm{k}^l)^2}{\frac{1}{\kappa}\ln(Ey^+)}Pr_tC_p^l \quad \textbf{2.46}$$

$$H^{l,Q} = \left(\frac{2}{\sqrt{\pi}}\sqrt{t^w\mathrm{k}^l\rho^lC_p^lf}\right)A^{2f} \quad \textbf{2.47}$$

So, the heat apportionment algorithm involves evaluation of the source terms in the energy equation (Equations 2.31 and 2.32) are computed at every iteration.

Specifically:

Step 1: Based on previous iteration values of computed temperatures, N''', d^B, f and are computed from Equations 2.41, 2.42, and 2.43, respectively.

Step 2: Effective area fractions A^{1f} and A^{2f} are computed from Equations 2.39 and 2.40.

Step 3: The wall heating that goes into evaporation, $q''^{,v,E}$, is computed from Equation 2.37.

Step 4: Sensible and quenching heat transfer coefficients, $H^{l,S}$ and $H^{l,Q}$ are computed from Equations 2.46 and 2.47.

Step 5: Evaporative mass transfer, Γ^{lv} , is determined from Equation 2.20.

Step 6: The new wall temperature, T^w, is computed using Equation 2.45 (after algebraic manipulation):

$$T^w = \frac{q''^{,w} - q''^{,v,E}}{(H^{l,S} + H^{l,Q})} + T^{l,bulk} \quad \textbf{2.48}$$

Step 7: Net wall heat to liquid is applied as:

$$q''^{,w,liq} = q''^{,l,S} + q''^{,l,S} = q''^{,w} - q''^{,v,E} \quad \textbf{2.49}$$

2.2.4 Crud Modeling

The focus of this thesis is on the extension of the clean-surface subcooled boiling model presented in the previous section to crudded surfaces. Based on the crudded boiling phenomenology presented in Chapter 1, a suitable set of additional physics to be considered are proposed:

1. Surface roughness

2. Crud layer conductivity
3. Surface boiling modifications including increased nucleation site density, increased nucleation frequency, and decreased bubble departure diameter
4. Wick boiling associated with “chimneys”

A dimensionally and physically consistent approach to modeling each of these is presented.

2.2.4.1 Surface Roughness

The surface deposits can be characterized as being hydrodynamically rough. In particular, depending on the nature of the sediments, irregularities in the surface arise that are larger in characteristic dimension than the smallest turbulence scales present ($y^+ = 1$). In this thesis, crud surface roughness is accommodated in a fashion consistent with the law-of-the-wall employed in the turbulence model. Specifically, in the $k - \varepsilon$ model, wall shear is modeled using the classic law-of-the-wall (Schlichting (23), for example). For smooth walls:

$$U^+ = \frac{1}{\kappa}\ln\left(Ey^+\right) \qquad \textbf{2.50}$$

where standard values are taken as $\kappa = 0.4187$ and $E = 9.793$ in this work. Following White (24), a modification is adopted to the law-of-the-wall to accommodate surface roughness:

$$U^+ = \frac{1}{\kappa}\ln\left(\frac{Ey^+}{1 + 0.3\mathrm{k}^+}\right) \qquad \textbf{2.51}$$

where k^+ is the characteristic surface roughness height in inner variables defined by:

$$k^+ = \frac{\rho k v^*}{\mu} \quad \textbf{2.52}$$

In Equation 2.52, k is the specified dimensional characteristic roughness height and v^* is the friction velocity defined in Equation 2.53.

$$v^* = \sqrt{\frac{\tau_w}{\rho}} \quad \textbf{2.53}$$

In concert with the Reynolds analogy, the attendant increase in heat transfer coefficient is accommodated by:

$$H^{l,S} = \frac{C_\mu^{\frac{1}{4}} \rho^l (k^l)^2}{\frac{1}{\kappa} \ln (E y^+)} Pr_t C_p^l \quad \textbf{2.54}$$

The turbulence parameters that appear in Equation 2.54 are defined with Equation 2.36.

2.2.4.2 Crud Layer Conductivity

As discussed in Chapter 1, crud layers can reach 1 mm (0.039 in) in thickness. Although often quite porous, the chemical makeup of these deposits have effective thermal conductivities ranging from 0.156 to 21.21 W/m-°K (0.09 to 14.0 Btu/hr-ft-°F).

We define:

$$\mathrm{k}^{crud} = {-q''^{,wall}} \Big/ \frac{T_{crud\ surface} - T_{clad\ surface}}{t^{crud}} \qquad \textbf{2.55}$$

So, in Equation 2.55 we are not yet considering additional crud related heat transfer effects that arise due to wall-normal convection processes in boiling (chimneys). A number of researchers have characterized k^{crud} experimentally (see Chapter 1). For the case studied in subsequent chapters, Cohen and Taylor (6), determined an approximate value for k^{crud} based on single phase data. Accordingly, in this thesis, a quasi-one-dimensional (Q1D) approximation to this effective insulating nature of crud is accommodated as follows. Referring to Figure 2.6, using the heat apportionment logic, $\Delta T^{crud} \equiv T^{wall} - T^{crud}$ is computed from $\Delta T^{crud} = \frac{-q''^{,wall}.t^{crud}}{\mathrm{k}^{crud}}$. This is computed for each heated wall face. In the heat apportionment algorithm, then, ΔT^{crud} is the "wall" temperature used to compute all three modes of boiling heat transfer (sensible, quenching, evaporation). Note that this approach is valid for single phase flow where, in the absence of nucleation, only sensible heating is modeled and the insulating effects of the crud gives rise to significantly higher wall temperatures. It should also be noted that since crud thickness is generally much smaller than channel heights, for constant wall heat flux conditions the single phase temperature field in the liquid is nearly unaffected by the insulating layer itself (although crud surface roughness impacts this convection process per the previous section).

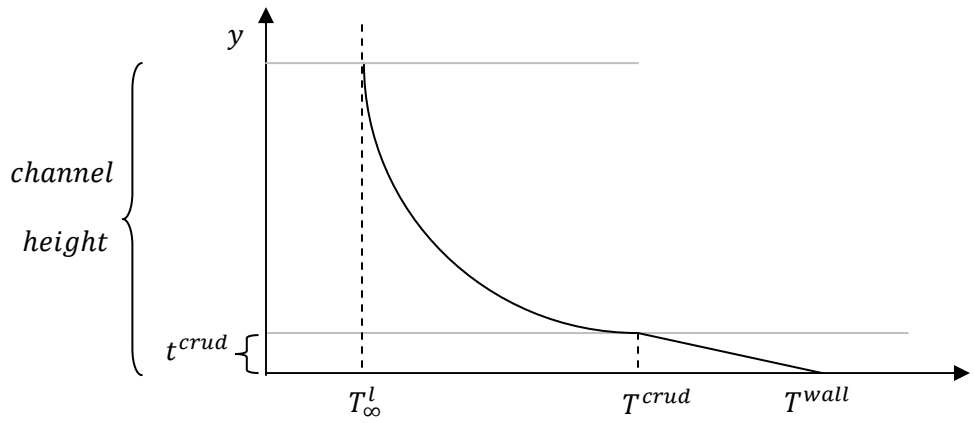

Figure 2.6: Temperature Change in a Heated Channel with Crud Present

2.2.4.3 Nucleation Modification

As discussed in Chapter 1, Cohen and Taylor (6) observed a larger number of nucleation sites and a smaller bubble departure diameter on crudded boiling surfaces compared to clean surface boiling. So, to model the crud, the nucleation site density, N''', will increase by a calibrated factor and the bubble diameter, d^B, will decrease by another calibrated factor. Changing nucleation site density and bubble diameter will effect the amount of evaporation and quenching present on the surface. The evaporative heat flux automatically increases when the nucleation site density increases (refer to Equation 2.37 in 2.2.3). On the other hand, quenching heat flux is only indirectly impacted by nucleation site density through A^{2f} (Equations 2.38 and 2.40 in Section 2.2.3). Because the relation is indirect, the quenching heat flux needs to be increased by a calibrated factor as well.

The factors for nucleation site density, bubble diameter, and quenching heat flux for a crudded surface were calibrated such that the Cohen and Taylor data (see Chapter 4) is well matched when used in conjuction with the wick boiling model. The resulting factors are summarized in Table 2.1.

Table 2.1: Calibrated Factors for Crud Model

Parameter	Factor
N'''	2
d^B	0.5
$q'''^{,l,Q}$	2

2.2.4.4 Wick Boiling

Referring to Chapter 1 and Figure 1.5, three parameters are proposed to characterize wick boiling:

1. Wall superheat (of the clad surface, not the crud surface) $\Delta T^{sup,crud} = T^{clad} - T^{sat}$
2. Pore site area density, M''
3. Characteristic pore diameter, D^{pore}

Also, it is conjectured here that the chimney ejection physics becomes vigorous (i.e. jet-like) only once vigorous boiling at the surface occurs. Accordingly, wick boiling onset wall superheat is proposed as another model parameter, i.e., ΔT^{onset}; for which no wick boiling occurs below this critical value of $\Delta T^{sup,crud}$.

In this work, the increased heat transfer due to wick boiling is implemented as an effective crud conductivity correction (i.e. increase):

$$k^{crud,effective} = k^{crud}\left[\left(\Delta T^{sup,crud} - \Delta T^{onset}\right)A^{w}\kappa + 1\right] \quad \textbf{2.56}$$

where A^w is a wick boiling area availability factor:

$$A^w = \pi(D^{pore})^2 M'' \kappa \quad \textbf{2.57}$$

and κ is a model calibration constant.

In the present work, representative values were taken: $D^{pore} = 10^{-5}\ m$ and $M'' = 5 \times 10^9\ m^{-2}$ from Cohen (5). These values would of course vary with crud characteristics. The calibration constant is taken to be $\kappa = 0.034$, which provides good agreement with experiment as shown in Chapter 4.

In the future, additional experimental data on crudded boiling could be used to refine the present model. In particular, the exponent on the wall superheat (taken as 1.0 here) could be calibrated to a higher number in order to account for a likely superlinear increase in chimney jetting and, thereby, heat transfer coefficient, with clad superheat. This would be consistent with the present (and other) nucleation site density models (Equation 2.41). Also, constant κ could be formulated using dimensional analysis to accommodate other system parameters that could be of importance in wick boiling. This includes crud porosity, crud thickness, liquid surface tension, h^f, h^g, ρ^f, ρ^g, and (per Cohen (5)) various other chemistry parameters.

2.3 **Numerics**

For single phase flow, the present algorithm follows established segregated pressure based methodology. A collocated variable arrangement is used and a lagged coefficient linearization is applied. One of several diagonal dominance preserving, finite volume spatial discretization schemes is selected for the momentum and turbulence transport equations. Continuity is introduced through a pressure correction equation, based on the SIMPLE-C algorithm (25). In constructing cell face fluxes, a momentum interpolation scheme (26) is employed which introduces damping in the continuity equation. For each iteration, the discrete

momentum equations are solved approximately, followed by a more exact solution of the pressure correction equation. Enthalpy, turbulence scalar, and volume fraction equations are then solved in succession. Several important numerical issues arise in two-fluid CFD, foremost among these, that sufficient implicit coupling between the constituents be established. In the present work this is accomplished using the Coupled Phasic Exchange (CPE) algorithm (27).

2.3.1 Discretization

The governing equations are discretized using a cell centered finite volume method applied to arbitrary polyhedral cell types.

Inviscid fluxes are evaluated from:

$$\int_{\vec{A}} \alpha^k \rho^k \phi^k \overrightarrow{V^k} \cdot d\vec{A}) \approx \sum_f C_f^k \, \phi_f^k \qquad \textbf{2.58}$$

Here, C_f^k is face mass flux for field *k*, and ϕ_f^k is the value of general transport scalar ϕ^k evaluated at face, f. The summation is taken over all faces bounding the element. C_f^k is evaluated based on field variables available prior to the solution of the transport equation for ϕ_f^k (lagged coefficient linearization). Second order accuracy is obtained by evaluating C_f^k using a central plus 4th difference pressure artificial dissipation term from Rhie and Chow (26):

$$C_f^k = \rho_f^k \alpha_f^k \overrightarrow{\overline{V^k}} \cdot \overrightarrow{A_f} + \rho_f^k \alpha_f^k \left[\overline{B^k} \left(\overline{\nabla p_f} \cdot \overrightarrow{A_f} - \Delta p \left| \overrightarrow{A_f} \right|^2 \right) \right] \qquad \textbf{2.59}$$

and by evaluating ϕ_f^k from (28):

$$\phi_{\mathrm{f}}^{k} = \phi_{\mathrm{U}}^{k} + \left(\nabla\phi^{k} \cdot \mathrm{d}\vec{\mathrm{r}}\right)_{\mathrm{U}} \qquad \textbf{2.60}$$

In Equation 2.59, the overbar denotes a geometrically weighted mean at the face, i.e. referring to Figure 2.7:

$$\overline{\nabla \mathrm{p}_{\mathrm{f}}} = (1 - \mathrm{s})(\nabla \mathrm{p}_1) + \mathrm{s}(\nabla \mathrm{p}_2) \qquad \textbf{2.61}$$

$$\mathrm{s} \equiv \frac{\delta \mathrm{s}_1}{(\delta \mathrm{s}_1 + \delta \mathrm{s}_2)} \qquad \textbf{2.62}$$

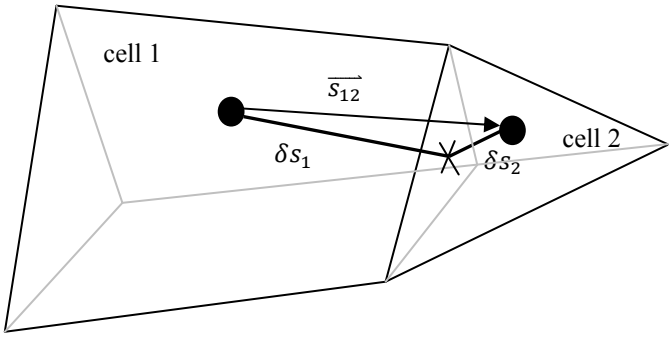

Figure 2.7: Geometry Nomenclature for Cell Face Evaluations

In Equation 2.59, Δ designates a difference across the face (i.e. $\Delta \mathrm{p} \equiv \mathrm{p}_2\text{-}\mathrm{p}_1$). In Equation 2.60, subscript U designates the quantity associated with the element upwind of face, f, and $\mathrm{d}\vec{\mathrm{r}}$ is the vector from the upwind cell center to the face center. The first order contribution in Equation 2.60, ϕ_{U}^{k} , is treated implicitly, the second order contribution explicitly.

Neglecting cross-diffusion and dilatation, the viscous flux in the momentum equations can be written for an element face as:

$$\int \left(\underline{\underline{\tau}} \cdot \mathrm{d}\vec{A}\right), \ \underline{\underline{\tau}} \equiv \alpha\mu(\nabla\vec{V}) \qquad \textbf{2.63}$$

Gradients that appear in the flux calculations, and elsewhere (pressure gradient and dispersion forces), are computed using Gauss' Law:

$$\nabla\phi = \frac{1}{\forall}\sum_{\mathrm{f}} \overrightarrow{A_{\mathrm{f}}}\,\phi_{\mathrm{f}}^{\mathrm{k}} \qquad \textbf{2.64}$$

with internal face values of $\phi_{\mathrm{f}}^{\mathrm{k}}$ computed from Equations 2.61 and 2.62, and the summation taken over all faces bounding an element. Equation 2.64 is computed by sweeping all internal and boundary faces, accumulating adjacent element contributions to $\forall$ and from the face.

2.3.2 Solution Procedure

The discretized governing equations for transport scalar, ϕ^{k}, can be written in Δ-form as ($\Delta\phi = \phi^{\mathrm{n+1}} - \phi^{\mathrm{n}}$):

$$\left[A_{\mathrm{P}}^{k} + \sum_{k\neq l} \mathrm{b}^{kl} + \frac{\rho^{k}\alpha^{k}\forall}{\Delta\tau}\right]\Delta\phi_{\mathrm{P}}^{k} - \sum_{k\neq l} \mathrm{b}^{kl}\Delta\,\phi_{\mathrm{P}}^{l} - \sum_{\mathrm{nb}} \mathrm{A}_{\mathrm{nb}}^{k}\Delta\,\phi_{\mathrm{nb}}^{k}$$
$$= \left[\sum \mathrm{A}_{\mathrm{nb}}^{k}(\phi_{\mathrm{nb}}^{k})^{\mathrm{n}} - \left(A_{\mathrm{P}}^{k} + \sum_{k\neq l} \mathrm{b}^{kl}\right)(\phi_{\mathrm{P}}^{k})^{\mathrm{n}}\right. \qquad \textbf{2.65}$$
$$\left. - \sum_{k\neq l} \mathrm{b}^{kl}(\phi_{\mathrm{P}}^{l})^{\mathrm{n}}\right] + \mathrm{S}^{k}$$

where A_{P}^{k} and A_{nb}^{k} represent the influence coefficients arising from convection and diffusion term discretization, associated with element P and its neighbors, nb. Here, b^{kl} represents the accumulated drag and mass transfer terms (i.e., for the momentum equations, $\mathrm{b}^{kl} = D^{kl} + \Gamma^{kl}$).

S^k represents all other source terms (e.g. momentum: buoyancy, pressure gradient, non-drag forces, energy: wall heating).

In Equation 2.65, Euler implicit differencing is employed for the pseudo-time derivative ($\Delta\tau$). A standard under-relaxation procedure is employed where an appropriate under-relaxation factor, ω is selected ($\omega \cong 0.7$) and the pseudo-timestep is evaluated from:

$$\Delta\tau = \frac{\omega}{1-\omega}\left(\frac{\rho^k \alpha^k V}{A_P^k + \sum_{k\neq l} b^{kl}}\right) \quad \textbf{2.66}$$

It has been observed in the work of Venkateswaran (29) that such a specification is equivalent to a local time-stepping procedure that accommodates CFL and Von Neumann stability.

2.3.3 Interfacial Force Evaluation

In order to discuss interfacial force discretization issues, we consider the two classes of these terms incorporated in this work. First, when cast as in Equation 2.2, drag can be viewed as a scalar sink term. That is to say, drag term, D^{kl}, which appears in the momentum equations as:

$$\sum_{k\neq 1} D^{kl}\,(u_i^l - u_i^k) \quad \textbf{2.67}$$

is by virtue of its relative velocity factor incorporated *implicitly* by solving the momentum equations for each phase simultaneously. (Specifically this means that the solution of Equation 2.65 for k = vapor and liquid is carried out in a coupled fashion.) It is noted that numerically, mass transfer plays a very similar role to drag (though $D^{kl} = D^{lk}$ and in general $\Gamma^{kl} \neq \Gamma^{lk}$), and

accordingly its treatment is consistent with that discussed for drag. The second class of interfacial force terms are those that are linear in the gradient of volume fraction. These are generally dispersive in nature. These terms are evaluated straightforwardly using Equation 2.12, however, as is demonstrated in (27), including a Rhie-Chow-like term (26), in Equation 2.59 is critical for obtaining convergent oscillation free solutions when such forces are present. Specifically, when the dispersion force, Equation 2.12 is added to the momentum equations, the cell face flux is computed as:

$$\begin{aligned} C_f^k = \rho_f^k \alpha_f^k \overline{\overline{V^k}} \cdot \overrightarrow{A_f} + \rho_f^k \alpha_f^k \left[\overline{B^k} \left(\overline{\nabla p_f} \cdot \overrightarrow{A_f} - \Delta p \left| \overrightarrow{A_f} \right|^2 \right) \right] \\ + \rho_f^k \left[\overline{F^k} \left(\overline{\nabla \alpha_f^k} \cdot \overrightarrow{A_f} - \Delta \alpha_f^k \left| \overrightarrow{A_f} \right|^2 \right) \right] \end{aligned} \quad \textbf{2.68}$$

2.3.4 Continuity Equation Linear Solution Strategy

In the present work a mixture volume conservation equation is derived by summing individual field volume fraction equations, each normalized by field density. A SIMPLE-C (25) based pressure-velocity corrector relation is applied to develop an elliptic pressure correction equation. Transport equations for the field volume fraction equations are then solved. In this fairly standard method ((30), (31), (32), for example), under-relaxation is not employed for the pressure corrector equation in order to achieve a measure of mixture volume conservation at each pseudo-timestep. As a result, the discrete pressure corrector equation system is symmetric positive semi-definite ($A_P = \sum A_{nb}$) and thereby its linear solution is a challenging and important factor in the nonlinear convergence rate of the overall scheme. In the present work, a GMRES solver is employed through the PETSC solver library (33) for the solution of this system.

Chapter 3 Testing and Assessment of Two-Phase Heat Transfer Model

3.1 Case Description

The Eulerian two-fluid boiling model described in Chapter 2 was implemented in the NPHASE-PSU code ((18), (34), (35)). Once implemented, the model first had to be validated for clean surface boiling. In order to do so, a classic experimental data set from Bartolemei ((16), (17)) was used. Bartolemei studied boiling flow through a vertical tube with a 2 meter long heated length and an inner diameter of 15.44 mm (0.61 in). A number of mass fluxes, inlet subcoolings, and uniform heat fluxes were run in the facility. Measurements of wall temperature, average volume fraction, and average liquid temperature vs. axial coordinate were made. Another benefit to validating the model against the Bartolomei data is that Krepper et al. (9) recently studied this case using a similar heat apportionment algorithm to the one developed in this research. This enabled comparison of these simulations with Krepper's results as well.

An online ASME software program (36) was used to calculate the input parameters for h^{sat}, Pr^{l}, and μ at a quality of zero and one for liquid and vapor respectively. The particular case selected for study had the parameters listed in Table 3.1.

Table 3.1: Test Parameters Selected for Study from Bartolomei Experiment

System Pressure [MPa]	4.000
Mass Flux [kg/m^2-s]	900.000
Heat Flux [W/m^2]	570000
T^{sat} [ºK]	530.59
ΔT^{sub} [ºK]	58.2
T^{inlet} [ºK]	472.389
μ^l [Pa-s]	0.000103
d^{fl} [mm]	15.44
A^{inlet} [mm^2]	187.2339
mdot [kg/s]	0.169
$\rho^l = \rho^{l,sat}$ [kg/m^3]	787.61
$\rho^v = \rho^{v,sat}$ [kg/m^3]	22.7
ρ^{inlet} [kg/m^3]	867.79
h^f [kJ/kg]	1122.14
h^g [kJ/kg]	2798
$C_p^{\ l}$ [kJ/kg-K]	4.949
Pr^l	0.8356
k^l [W/m-K]	0.6088
V^{inlet} [m/s]	1.1427

The mass flow rate, $\dot{m}$, liquid density, ρ^l, and cross-sectional area, A^{inlet}, lead to:

$$V^{inlet} = \frac{\dot{m}}{\rho^l A^{inlet}} = 1.1427\ m/s \qquad \textbf{3.1}$$

which corresponds to a Reynolds number of:

$$Re_D = \frac{\rho^l V^{inlet} \mathrm{D_h}}{\mu^l} = 134{,}912 \qquad \textbf{3.2}$$

where $\mathrm{D_h} = \mathrm{D_o} - \mathrm{D_i}$.

3.2 CFD Model

An axi-symmetric model was developed with 20 grid cells radially and 80 grid cells axially. Uniform cell spacing was used in both directions. This choice led to y^+ values at the wall of approximately 75 along the entire duct, indicating that the mesh is appropriate for use with wall functions, i.e., $30 \leq y^+ \leq 300$. The choice of 80 axial cells arose from a grid study where the number of axial cells was successively doubled - the average volume fraction and temperature vs. x, was nearly indistinguishable from the 40 axial cell case.

In Figure 3.1, the predicted passage averaged volume fraction is plotted vs. x. Clearly, both the present analysis and the results published by Krepper et al. (9) correspond closely with the experiment. In particular, the slow increase in passage average volume fraction starting near the inlet, followed by a rapid increase near the exit is captured. Note that subcooled boiling is initiated quite close to the inlet with approximately 10% of the wall heat going into vaporization at $x = 0.5\ m$ (1/4 way through the heated section). It is the author's experience that this "tail-up" feature is difficult to capture with simpler boiling models, where all wall heat is transferred to the liquid and interfacial evaporation models are responsible for the boiling. There, one cannot directly distinguish between sensible heating and quenching, nor straightforwardly accommodate wall physics (e.g., nucleation site density). This leads to much more linear $< \alpha > vs. x$ boiling behaviour than observed.

The predicted temperature field is compared against the Bartolomei data in Figure 3.2. There channel averaged temperatures are compared. Very good correspondence between model and measurement are seen. One can observe the "tailing off " of the average temperature near the pipe exit, as the boiling becomes quite vigorous and much of the wall heat is expended in vapor formation. Also included in the plot is the near wall temperature (cell center of the wall adjacent node), which gives an indication of the narrowing of the wall heat and bulk temperature due to boiling.

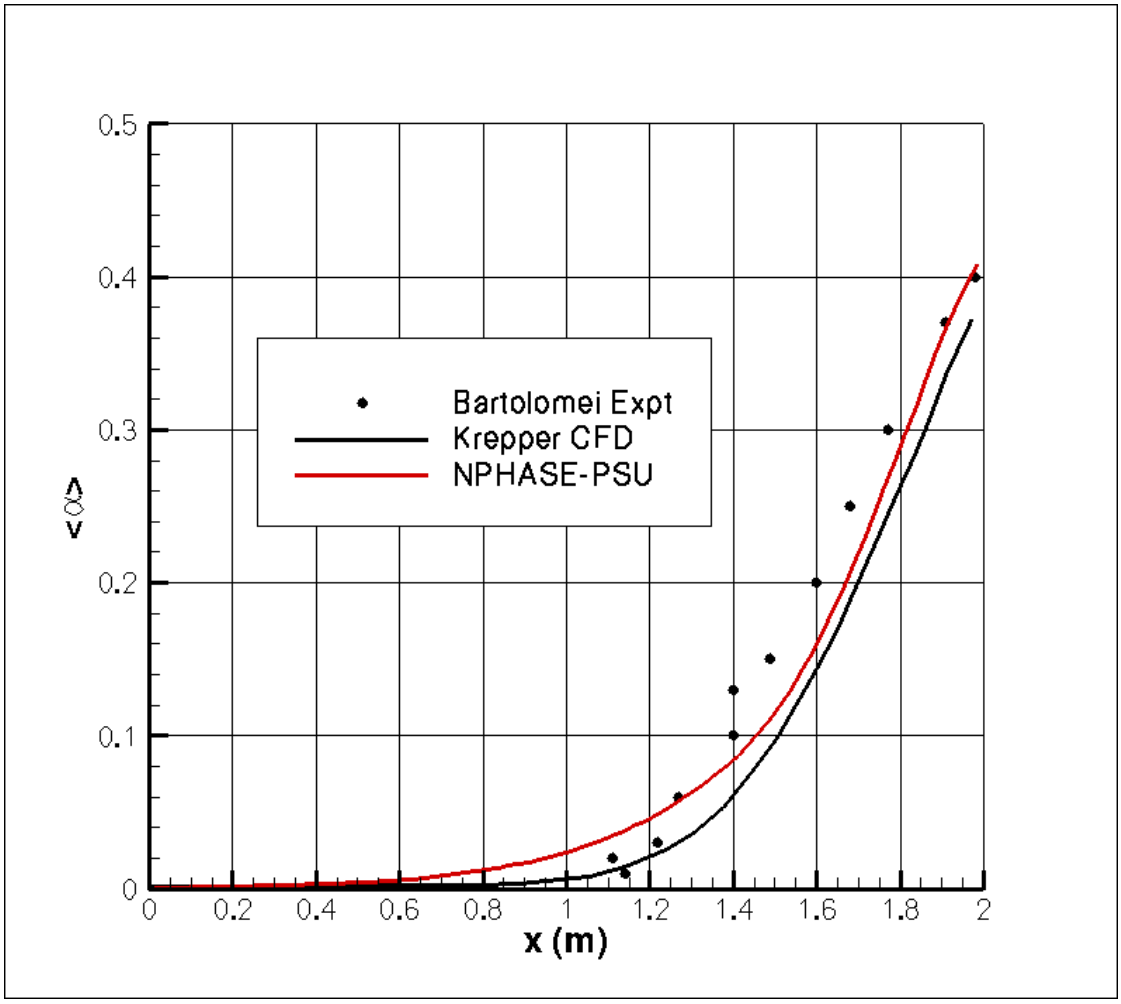

Figure 3.1: Channel averaged vapor volume fraction vs. x. Data due to Bartolomei (16), present results, and CFD results due to Krepper et al. (9)

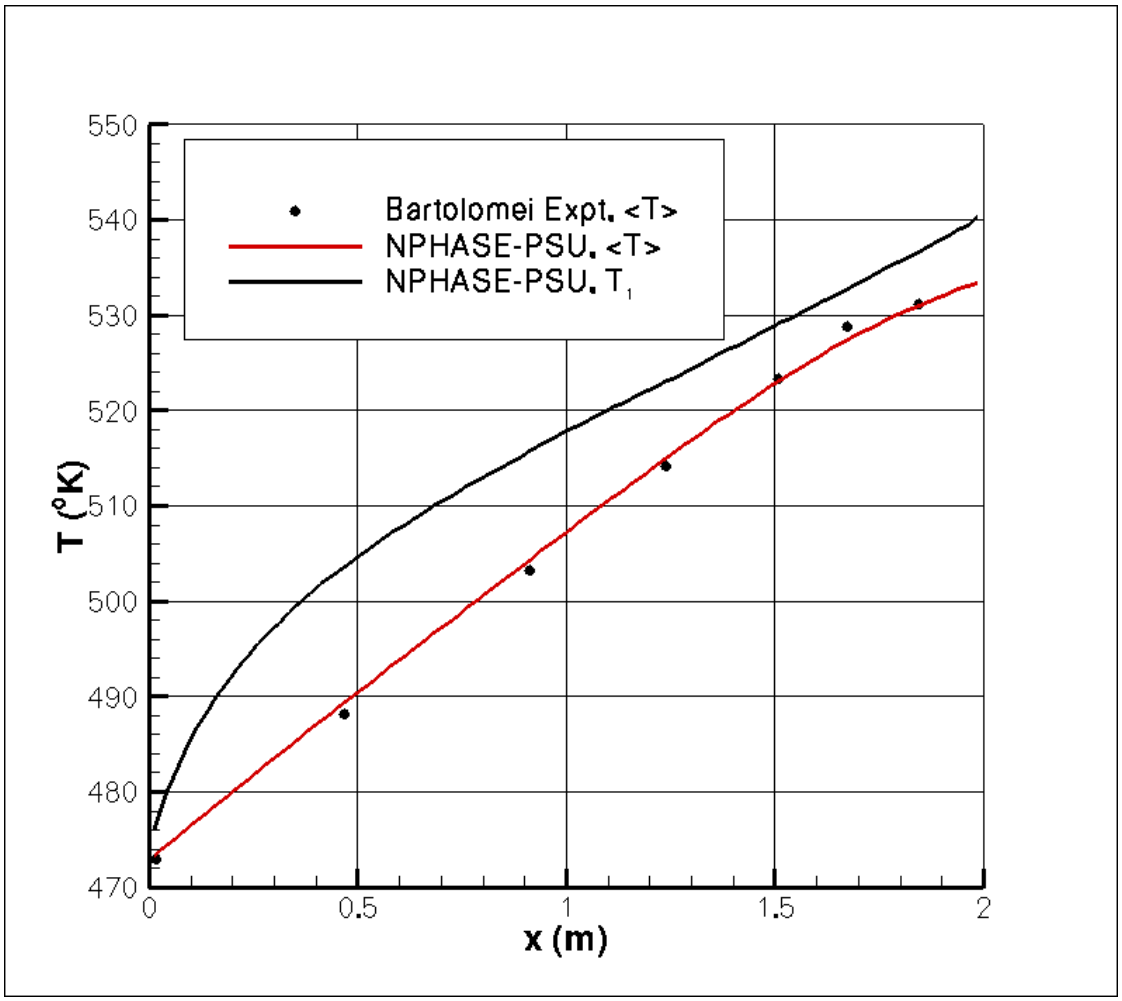

Figure 3.2: Channel averaged liquid temperature vs. x. Data due to Bartolomei (16). Present results include the channel average and the near-wall temperature.

In Figure 3.3 through Figure 3.5 qualitiative two-dimensional features of the flow are shown. In Figure 3.3, liquid temperature contours are shown. Note that the radial coordinate is scaled by a factor of 100 here. The saturation temperature contour ($T^{sat} = 530.56\,°K$) is indicated in black. Note that the predicted wall temperature is higher than saturation along most of the length of the duct, but since a wall function mesh is shown, this does not appear in the contours as the wall temperature is not explicitly solved for, but rather incorporated in the

enthalpy source term for wall adject cells (Equation 2.3). One can see that subcooled nucleate boiling exists through almost the entire length of the pipe.

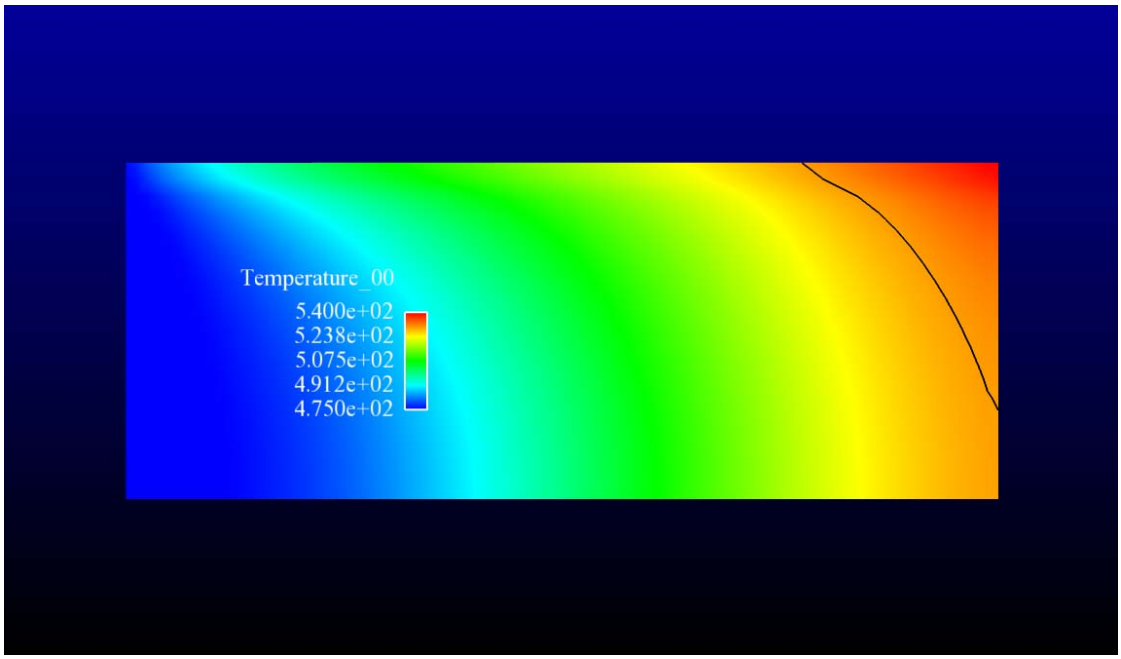

Figure 3.3: Predicted Contours of Liquid Temperature

Figure 3.4 shows predicted contours of vapor volume fraction. Again, one can see the ”concave” nature of the subcooled nucleate boiling process, where, comparing with Figure 3.3, much more vigorous boiling arises as the bulk flow becomes saturated.

Lastly, in Figure 3.5, contours of condensation mass transfer, Γ^{vl}, are shown. The behaviour of this model is quite interesting, being driven by both local subcooling and vapor (i.e., donor) mass fraction. As boiling begins to develop in the channel, virtually all of the vapor condenses (compare Figure 3.4) since the subcooling (and thereby the condensation rate) is high. The condensation rate reaches a maximum near the point where vigorous boiling begins (i.e. lots of donor phase available) and significant subcooling also exists. Condensation is seen to

diminish towards the exit of the channel, where the liquid approaches saturation (compare Figure 3.3) and towards the channel centerline, where very little vapor remains (Figure 3.4).

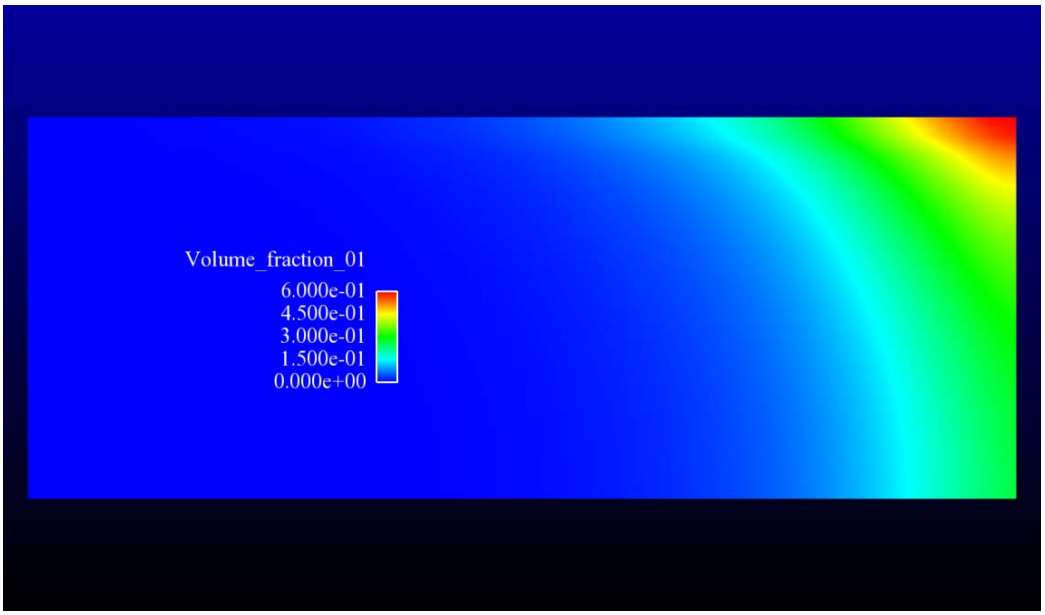

Figure 3.4: Predicted Contours of Vapor Volume Fraction

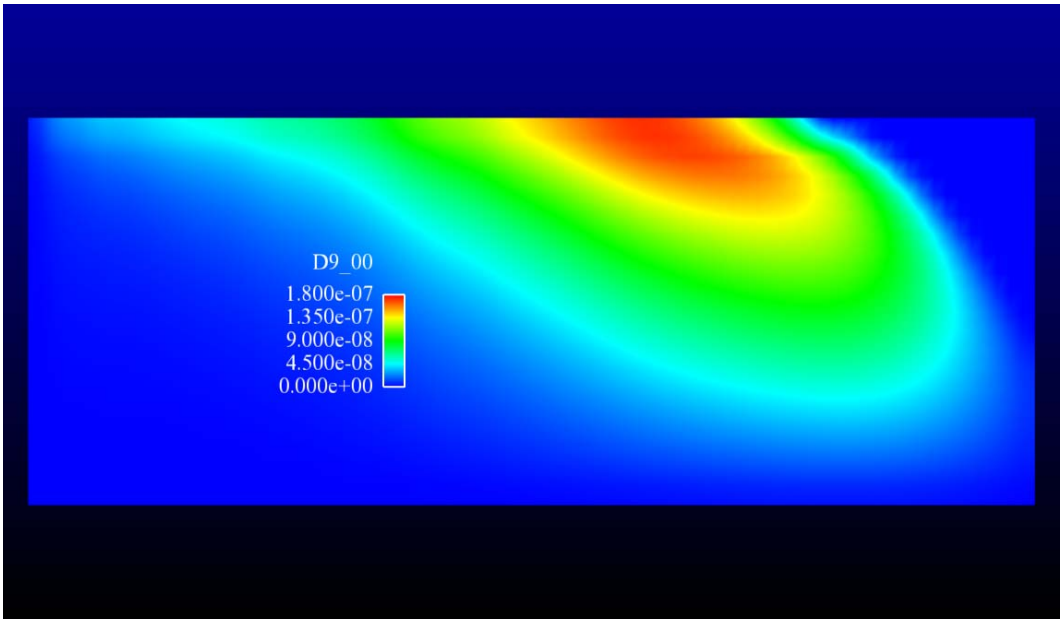

Figure 3.5: Predicted Contours of Condensation Rate

Chapter 4 CFD Analysis of Clean and Fouled Surfaces

In this chapter, the crudded boiling model presented in Chapter 2 is calibrated and assessed.

4.1 Description

As discussed in Section 1.4, Cohen and Taylor (6) documented the effects of porous deposits of magnetite on forced convection heat transfer in subcooled nucleate boiling. This is one of the only available published set of data on the performance of boiling crudded heat exchangers. Results of subcooled temperatures between clean and crudded surfaces at varying heat fluxes were compared. The saturated temperature of the test was $T^{sat} \sim 394.3$ °K (250 °F) (6) corresponding to $P^{sat} = 0.2057$ MPa (29.8 psi). It is clear that this pressure is much lower than the operating pressure of a typical PWR (~15.5 MPa/ 2250 psi).

The test included a hollow cylinder heated electrically with an internal thermocouple placed on the metallic surface of the specimen. The porous deposit that formed from precipitated deposits was 25.4 μm thick (1 mil) with a thermal conductivity, k, of 0.864 W/m-°K (0.5 Btu/hr-ft-°F). Cohen and Taylor reported linear regression fits of this test that can be seen in Figure 4.1.

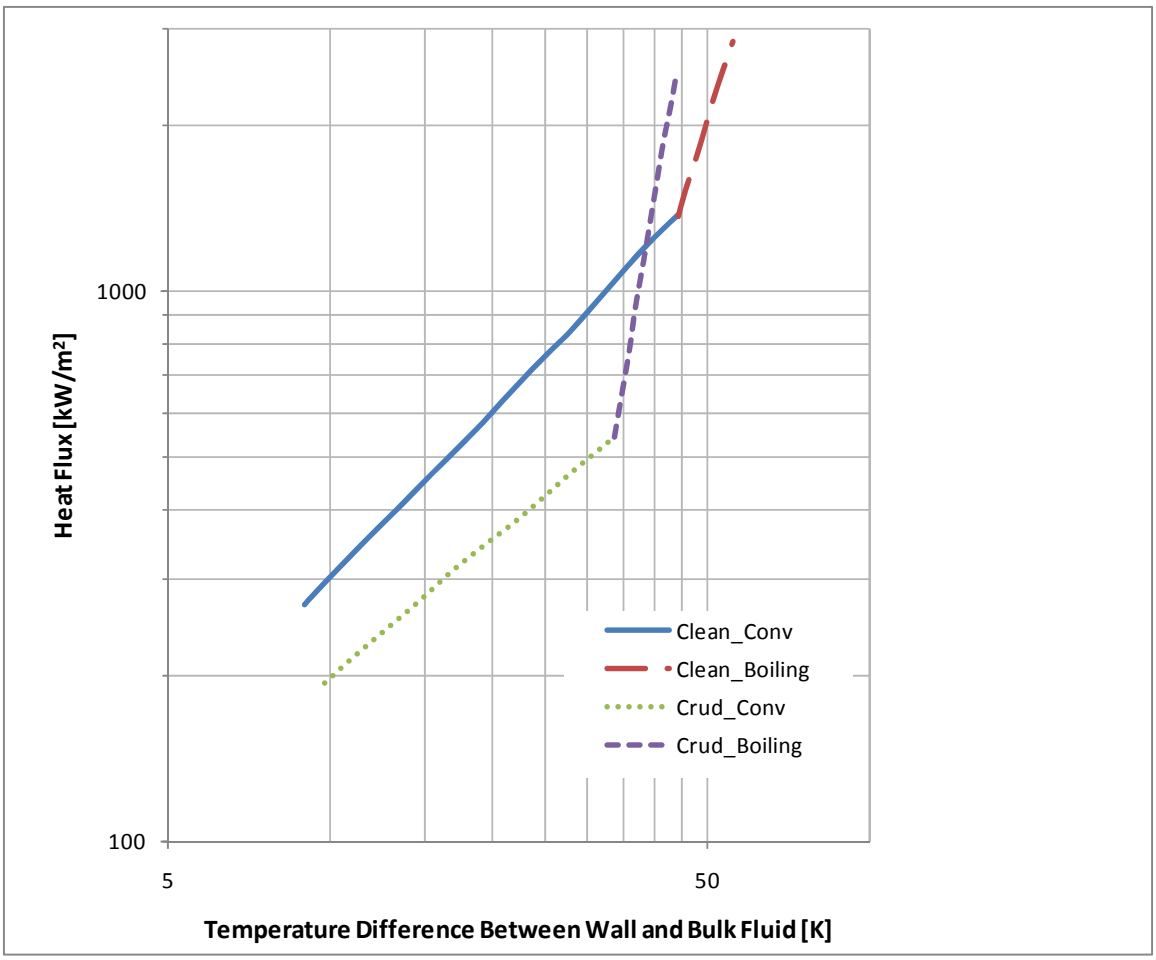

Figure 4.1: Subcooling Temperatures on Clean and Fouled Surfaces with Varying Heat Flux

4.2 **CFD Model**

A CFD model was created to compare to the results of Cohen and Taylor (6). Exact geometry of the test was not reported, but the authors of the test are cited to be from Westinghouse Electric Corporation. Because of this, the geometry of a Model 412 Westinghouse PWR was assumed and is summarized in Table 4.1.

Table 4.1: Geometry of CFD Model Based on Westinghouse PWR

Parameter	Dimension
Fuel Pin Diameter	9.5 mm/0.374 in (37)
Active Fuel Length	3.658 m/12 ft (37)
Rod Pitch	12.6 mm/0.5 in (3)

To determine the flow parameters to be used in the CFD input file some analysis was completed. A typical flow channel in thermal hydraulic analysis is square. An annular cross-section was used to approximate this shape in order that axisymmetric modeling could be employed. The flow area of the subchannel was conserved during this transformation as seen in Figure 4.2. Equation 4.1 was used to calculate the outer diameter of the annulus.

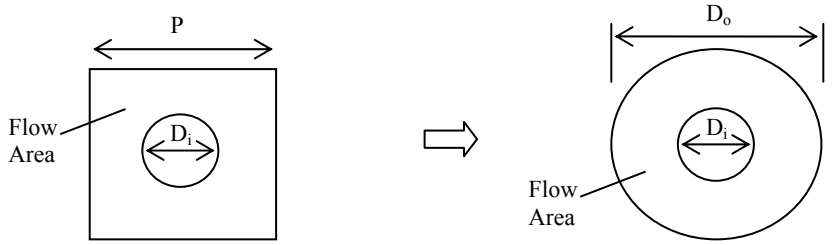

(a) Square Subchannel
A^{flow} = 87.98 mm^2
P = 12.6 mm

(b) Annulus
A^{flow} = 87.98 mm^2
D_o = 14.22 mm

Figure 4.2: Conserving Flow Area of Subchannel

$$P^2 + \frac{\pi D_i^2}{4} = \frac{\pi D_o^2}{4} - \frac{\pi D_i^2}{4} \qquad \textbf{4.1}$$

The final chosen geometry is illustrated in the axi-symmetric model of the flow channel in Figure 4.3. A uniform heat flux was applied to the inner wall as seen in the figure. To reiterate values from Table 4.1, the outer radius, $r_o = 7.1 \times 10^{-3}\ m$, the inner radius, $r_i = 4.75 \times 10^{-3}\ m$, and length, $L = 3.658\ m$.

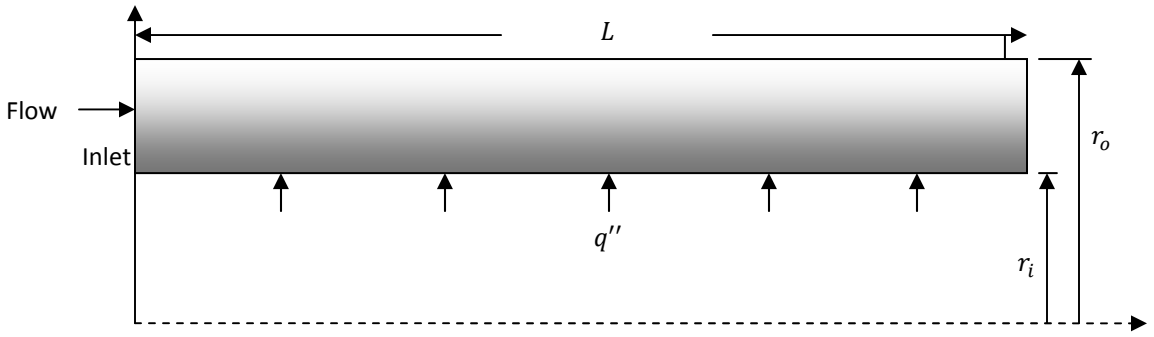

Figure 4.3: Axi-symmetric Model of Flow Channel

An online ASME software program (36) was used to calculate the input parameters for h^{sat}, Pr^l, and μ at a quality of zero and one for liquid and vapor respectively. Assuming 50 °K (90 °F) of subcooling, the inlet enthalpy was found using Equation 4.2 with software table values for h^{sat} and C_p^l. The remaining parameters summarized in Table 4.2 were calculated using Equations 4.3 through 4.5.

Enthalpy Equations:

$$\mathrm{h^{inlet}} = \mathrm{C_p^l}\left(-\Delta \mathrm{T^{sub}}\right) + \mathrm{h^{sat}} \qquad \textbf{4.2}$$

Reynolds Number:

$$Re_D = \frac{\rho^l V^{inlet} \mathrm{D_h}}{\mu^l}, \text{where } \mathrm{D_h} = \mathrm{D_o} - \mathrm{D_i} \quad \textbf{4.3}$$

Equations 4.4 and 4.5 were used to determine turbulence parameters k^{inlet} and ε_∞.

Turbulent Intensity: (For fully developed flow $\mathrm{T_{inlet}} \cong 0.15$)

$$\mathrm{T_{inlet}} = 0.15 = \sqrt{\frac{(2/3)\mathrm{k^{inlet}}}{\mathrm{V^{inlet}}}} \quad \textbf{4.4}$$

Epsilon Equation:

$$\varepsilon_\infty = \frac{\mathrm{C_\mu^{3/4}} \mathrm{k^{inlet}}^{3/2}}{\mathrm{L_\infty}} \quad \textbf{4.5}$$

where $\mathrm{C_\mu} = 0.09$ and $\mathrm{L_\infty} = 0.15 * \text{Channel Height}$

Adopting an approximate geometry is sufficient for the present assessments since, for the given applied heat flux, an inlet subcooling and mass flow rate can be assumed such that the local difference between wall temperature and bulk fluid temperature ($T^w - T^{l,bulk}$) will match Cohen and Taylor's data at some axial distance downstream from the inlet. Here, we adopted an inlet subcooling of 50 °K and adjusted the inlet velocity such that the single phase ΔT_0 corresponded to Cohen's data at $x = L = 3.658$. For the geometry described above, this translates to $V^{inlet} = 9.09\ m/s$. This process is described in the next section.

Table 4.2: Inlet Parameters for CFD Model

T^{sat} [K]	394.3
T^{sub} [^oK]	50
T^{inlet} [^oK]	344.3
P^{sat} [MPa]	0.2057
A^{inlet} [mm^2]	87.932
mdot [kg/s]	0.321
$\rho^l = \rho^{l,sat}$ [kg/m3]	942.22
$\rho^v = \rho^{v,sat}$ [kg/m3]	1.16
μ^l [Pa-s]	0.0002298
C_p^l [kJ/kg-K]	1.290
C_p^v [kJ/kg-K]	6.867
h^f [kJ/kg]	508.49
h^g [kJ/kg]	2707.5
h_{inlet} [kJ/kg]	444.010
Pr^l	1.0428
k^l [W/m-K]	0.683

4.3 **Matching Single Phase Results on Clean Surface**

To begin the comparison between experimental and CFD results, the clean single phase convection case was run with a mass flow rate of 18,000 kg/s. The temperature difference was recorded where the flow became fully developed corresponding to an axial location of 1.829 m. The CFD results were compared to Cohen and Taylor's experimental results from Westinghouse (6) and are shown in Figure 4.4.

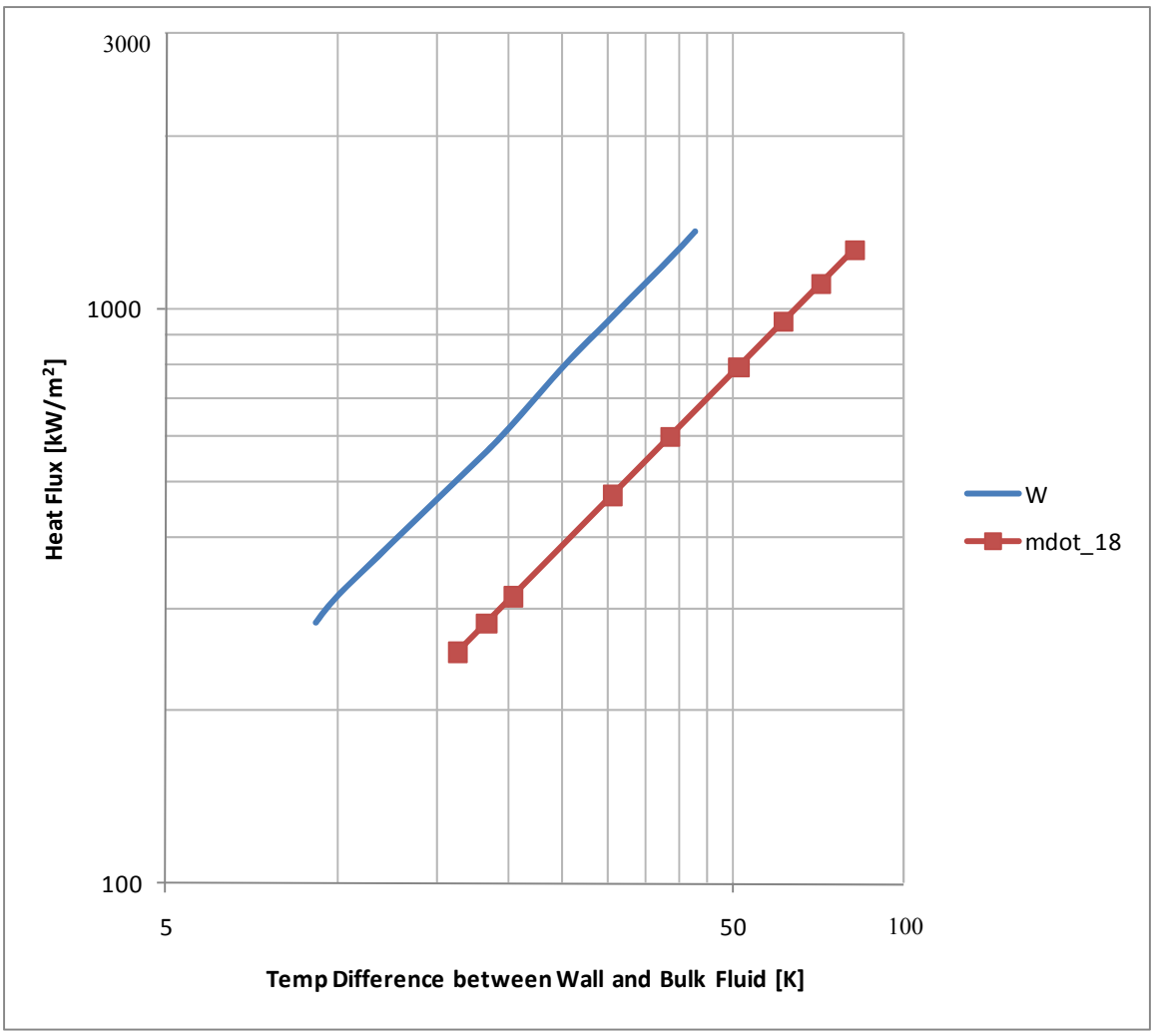

Figure 4.4: Comparing Single Phase Results on a Clean Surface (Experimental = W, CFD = mdot_18)

To match the Cohen and Taylor results, the single phase CFD curve needs to shift to the left. The difference in temperature between the wall and bulk fluid needs to decrease for this to happen. This is done by increasing the initial mass flow rate of the fluid. (Note: Since the inlet parameters were not given in the literature, inlet parameters were varied to match the single phase results. The parameters used to match the single phase results on a clean surface will be used for the clean two-phase case and the cases with crud deposits.)

After performing a study to vary the mass flow rate, it was found that a mass flow rate of 42,000 kg/s will allow the single phase convection results from CFD to match the experimental results quite well. Figure 4.5 shows the curve shifts to the left with increasing mass flow rate and matches with experimental results. The input parameters used for this flow rate are in Table 4.3 and will be the final input parameters used for CFD comparison.

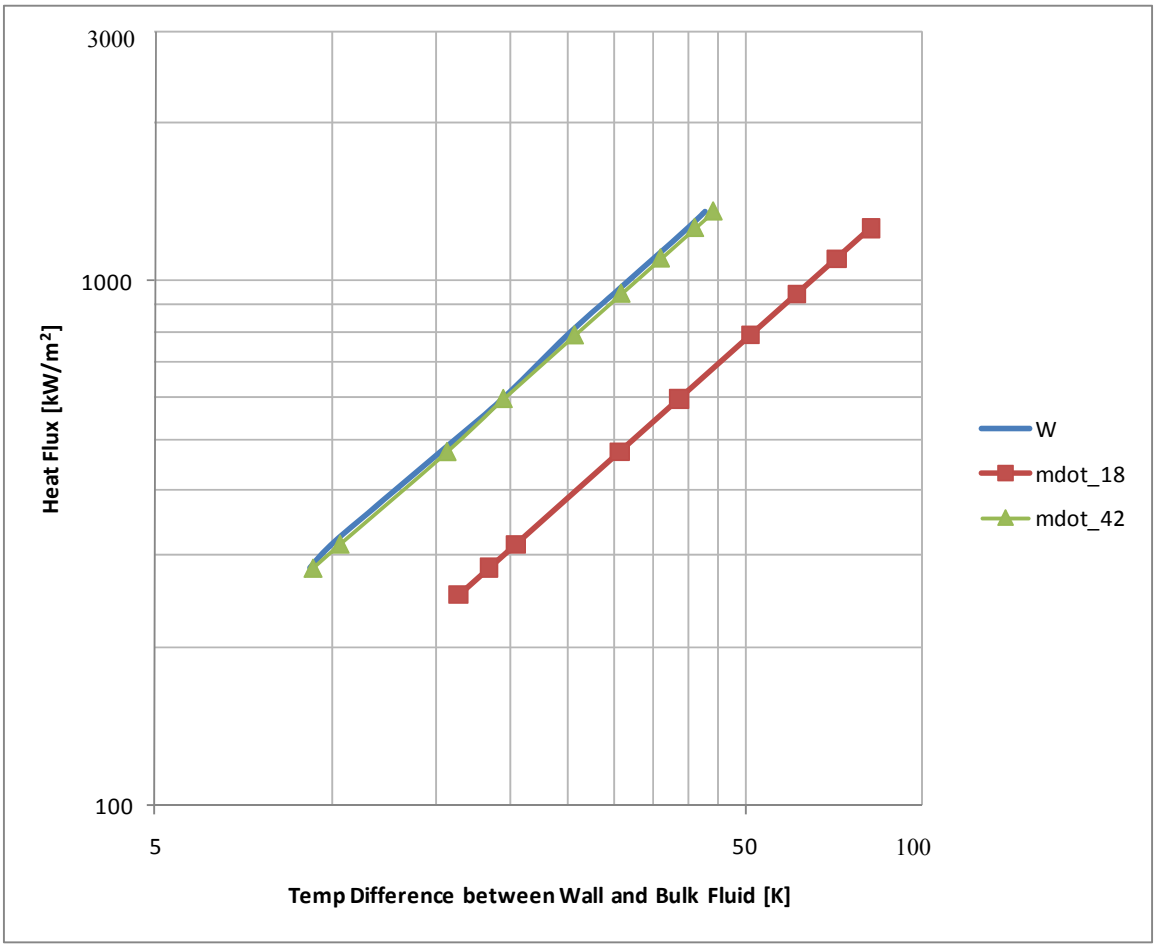

Figure 4.5: Matching Single Phase Results on a Clean Surface (Experimental = W, CFD = mdot_18, mdot_42)

Table 4.3: Input Parameters for CFD Model

T^{sat} [K]	394.3
T^{sub} [°K]	50
T^{inlet} [°K]	344.3
P^{sat} [MPa]	0.2057
A^{inlet} [mm^2]	87.932
mdot [kg/s]	0.753
$\rho^l = \rho^{l,sat}$ [kg/m3]	942.22
$\rho^v = \rho^{v,sat}$ [kg/m3]	1.16
μ^l [Pa-s]	0.0002298
$C_p^{\ l}$ [kJ/kg-K]	1.290
$C_p^{\ v}$ [kJ/kg-K]	6.867
h^f [kJ/kg]	508.49
h^g [kJ/kg]	2707.5
h_{inlet} [kJ/kg]	444.010
Pr^l	1.0428
k^l [W/m-K]	0.683

Given the system conditions listed in Table 4.3, Figure 4.6 is a plot of heat flux verse axial length of the test section for an equilibrium quality of zero. As seen in the figure, if the applied heat flux is low ($\cong 8 \times 10^5\ W/m^2$) little or no boiling will be present at the very end of the test section ($\cong 3.5\ m$). Some local subcooled boiling may exist at these conditions, though. On the other hand, if the heat flux exceeds $\cong 3 \times 10^6\ W/m^2$, boiling begins towards the beginning of the test section and intense boiling may exist in the heated channel. If intense boiling occurs, the boiling models used in this research are no longer accurate.

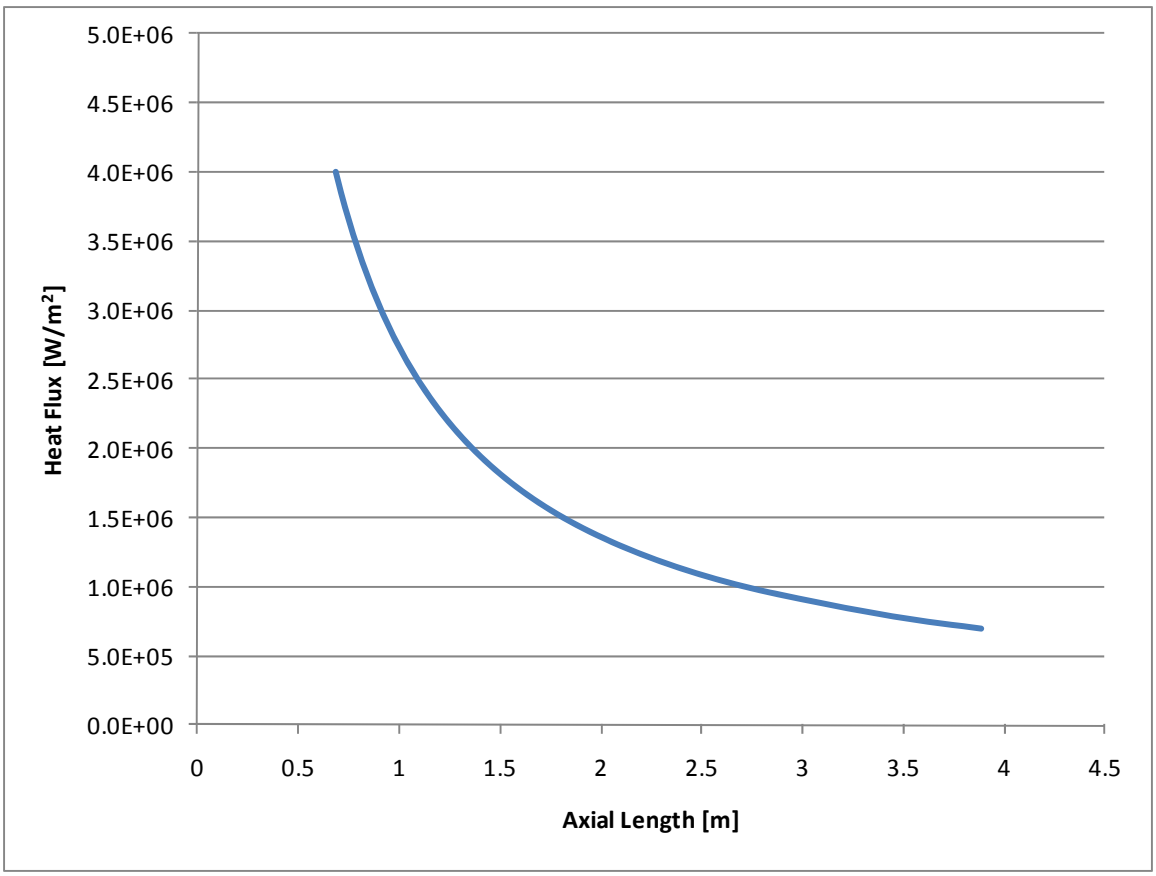

Figure 4.6: Heat Flux vs. Axial Length for Equilibrium Quality of Zero ($\langle x_e \rangle = 0$)

4.4 **Single Phase Results**

The single phase results for a clean surface are graphed in Figure 4.7 where it is seen that the NPHASE-PSU results match almost exactly with the experimental results. Convective heat transfer data can be correlated in terms of Re, Pr, and Nu. The Dittus-Boelter correlation is recommended for water flowing through long, straight, circular tubes. This correlation is shown in Equation 4.7 and is graphed against the data in Figure 4.7. The Dittus-Boelter line has the same slope as the experimental and NPHASE-PSU results showing our data is qualitatively correct.

$$Nu = 0.023Re^{0.8}Pr^{0.4} \quad \textbf{4.6}$$

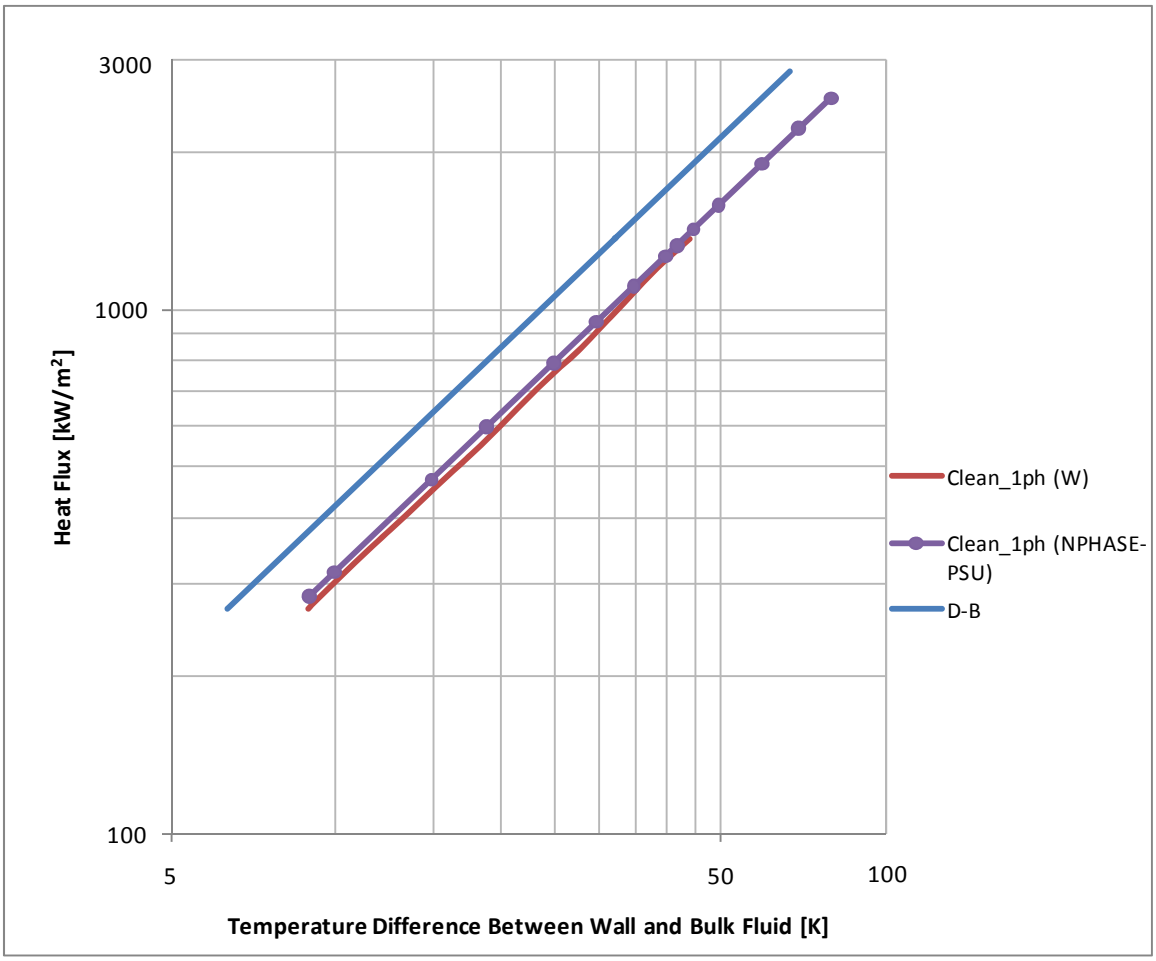

Figure 4.7: Single-Phase Results for Clean Surface

After analyzing the single phase crud results from Figure 4.1, it was concluded that the experimental results can be determined from the CFD results of the clean rod using a one dimensional heat transfer correction using Equation 4.7.

$$q'' = \frac{k^{crud}\Delta T^{crud}}{t^{crud}} \quad \textbf{4.7}$$

With a crud thickness, t^{crud}, of 30.05μm (0.0012 in), roughness of 0.00001 m (0.00093 in), and thermal conductivity, k^{crud}, of 0.864 W/m-°K (0.5 Btu/hr-ft-°F) (6), we can solve for the temperature difference between the wall and bulk fluid for the single phase crud case using the single phase clean NPHASE-PSU results. Figure 4.8 shows the results of this analysis.

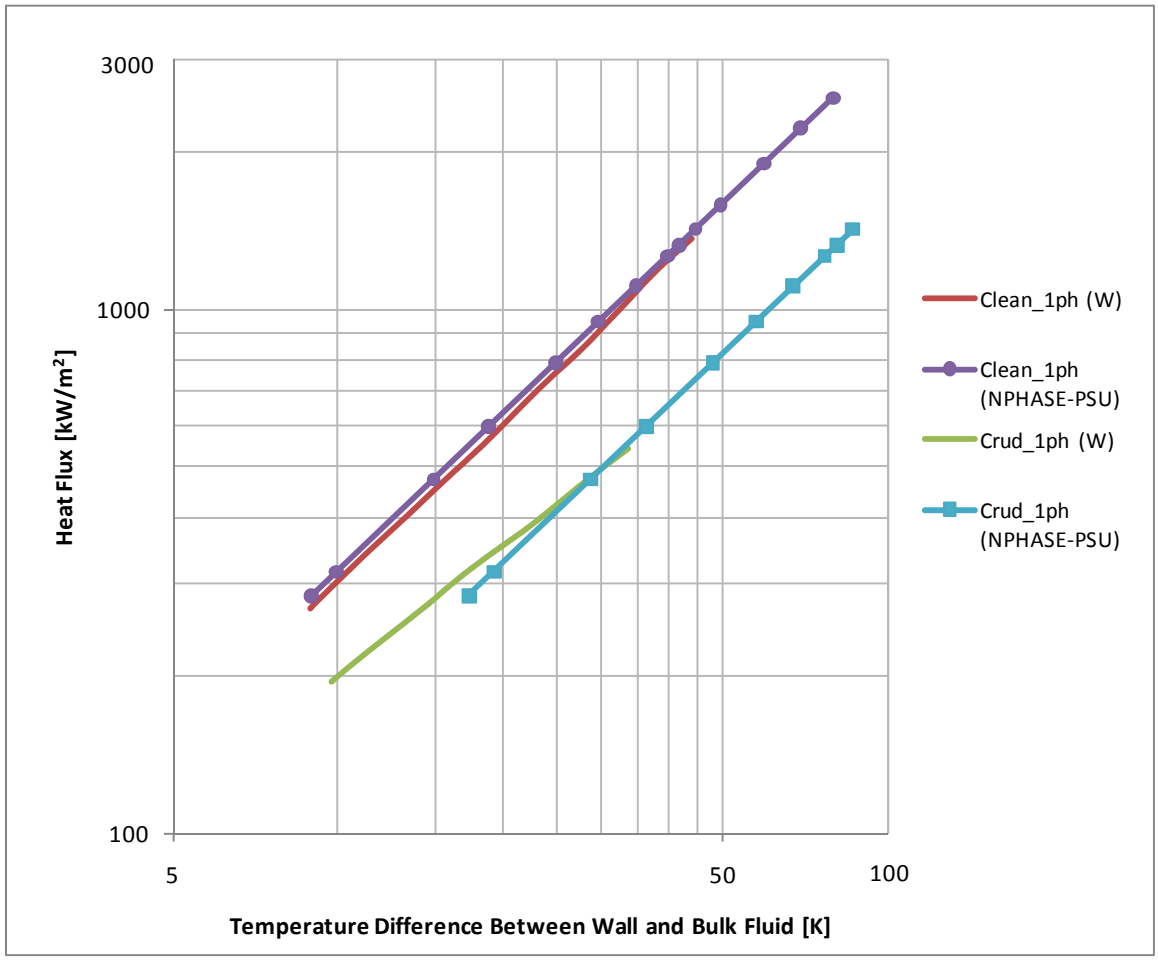

Figure 4.8: Single Phase Results for Clean and Crudded Surfaces

From the results, it is seen that there is a slope difference between the single phase experimental results and CFD results for a crudded surface. Some attributes of the crud are not accounted for in the 1-D heat transfer correction that was applied which could account for this slope difference. Specifically, in reality, thickness of crud varies along the axial length of the rod

as in Figure 4.9 (2). This is because boiling regimes change through the length of the reactor core. Subcooled nucleate boiling occurs in the top grid span of some assemblies and is the primary mechanism for crud deposition. For this reason crud becomes thicker at the top of the core. The experimental crud results in Figure 4.8 could have varying thickness, but only a single thickness is reported. The 1-D correction factor from Equation 4.7 does not account for varying crud thickness. Taking the variation of crud thickness into account in the CFD results could lead to a better match to the experimental data.

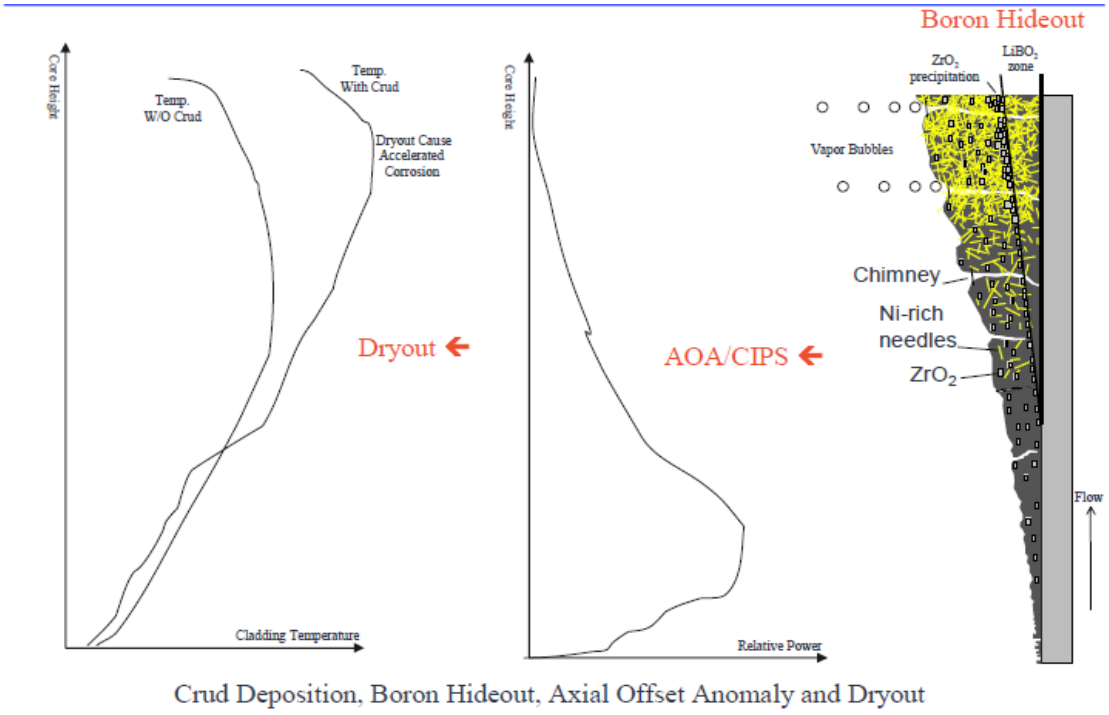

Figure 4.9: Variation of Crud Thickness along Core and Resulting Temperature

4.5 **Two Phase Results**

Using the two-phase heat transfer model developed in Section 2.2, the NPHASE-PSU results were compared to experimental data. Figure 4.10 shows the single phase results and two-phase results for both clean and crudded surfaces while comparing them to the experimental

results. From the figure it can be seen that the single-phase NPHASE-PSU results for a clean surface increase linearly. On the other hand, the two-phase results for a clean surface exhibit some non-linearity not evident in the linear experimental data regression. This being said, the general trend for the two-phase clean surface results follows that of the experimental results.

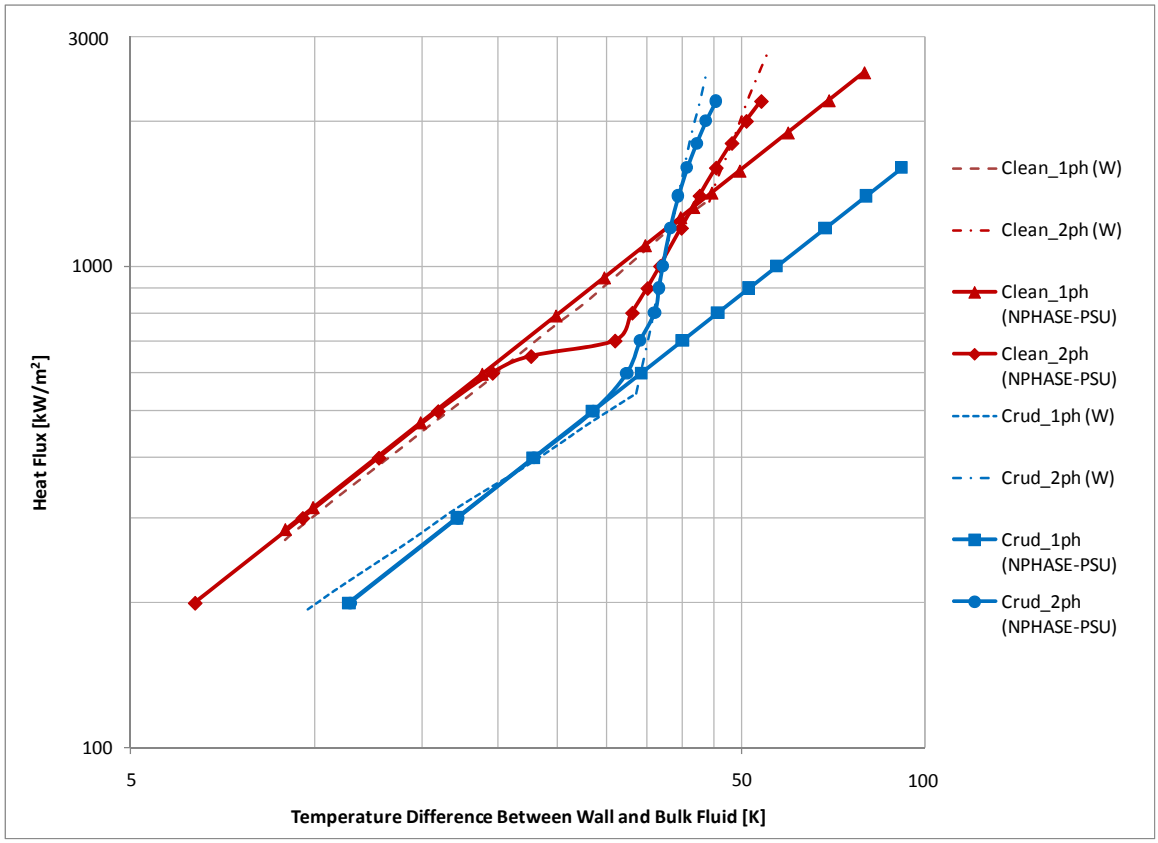

Figure 4.10: Experimental and NPHASE-PSU Results for One-Phase and Two-Phase

After applying the crud model described in Section 2.2.4, the two-phase results from NPHASE-PSU on a crudded surface match well with those from experiment. Figure 4.10 illustrates that the single phase and two-phase results for clean and crudded surfaces from NPHASE-PSU match experimental results validating the subcooled boiling heat transfer model and crud model developed. Additional figures from this analysis can be seen in Appendix A.

A study was performed to determine the effect of eliminating the wick boiling model described in Section 2.2.4.4. By neglecting this model, chimneys are no longer used as a means of heat removal in the crud. As seen in Figure 4.11, as expected, the temperature difference increases without the wick boiling model present. Boiling does occur and there is a similar non-linear behavior as seen in the two-phase case for clean surfaces. It can be concluded that chimneys developed in crud deposits are a major mechanism of heat removal on heated surfaces at high heat fluxes.

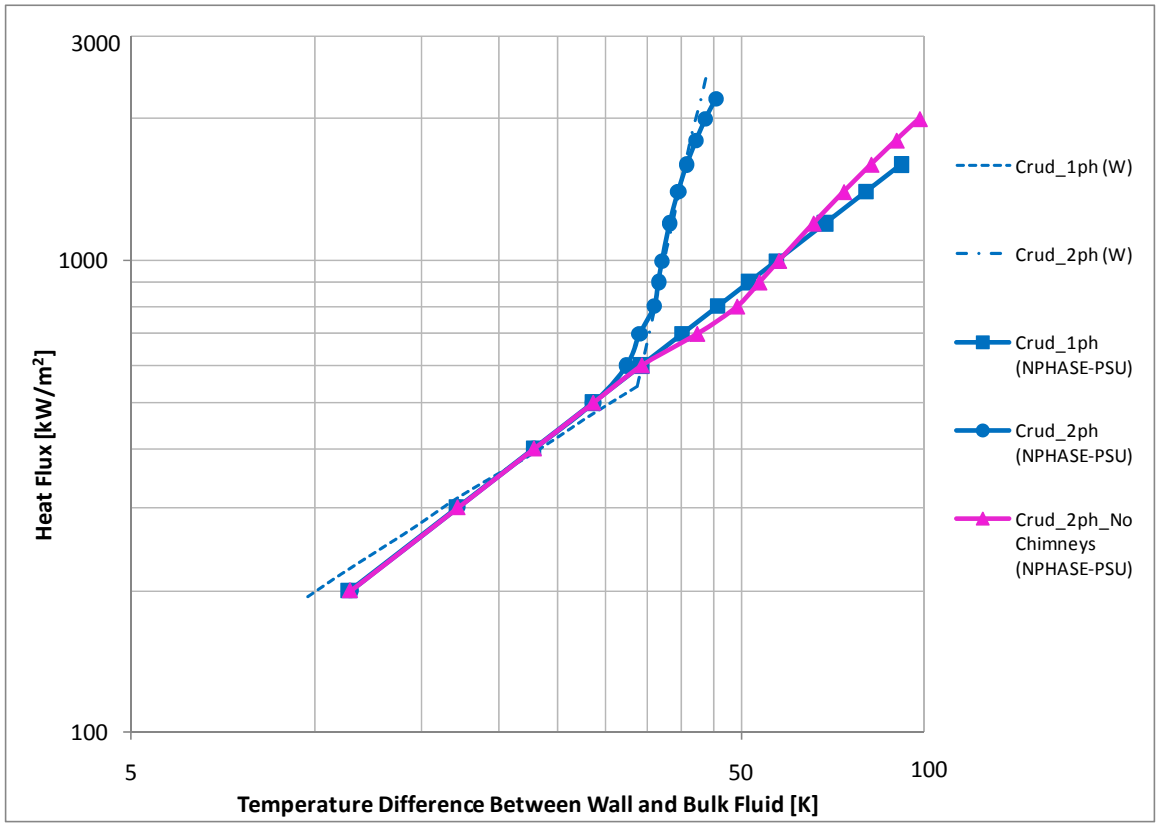

Figure 4.11: Boiling and Crud Model on and Chimney Model Off

Cohen (5) compared experimental results from various researchers studying boiling on crudded, heated surfaces with and without chimneys present. His results (Figure 4.12) show that the effective conductance (i.e. conductivity) of the crud increases drastically when chimneys are

present under boiling conditions. This is consistent with the new wick boiling model (presented in 2.2.4.4). From Equation 4.7, ΔT^{crud} is linearly related to k^{crud}, so, as k^{crud} increases, ΔT^{crud} decreases. This can be directly attributed to the temperature effect seen in Figure 4.12. Additional figures from this analysis can be seen in Appendix A.

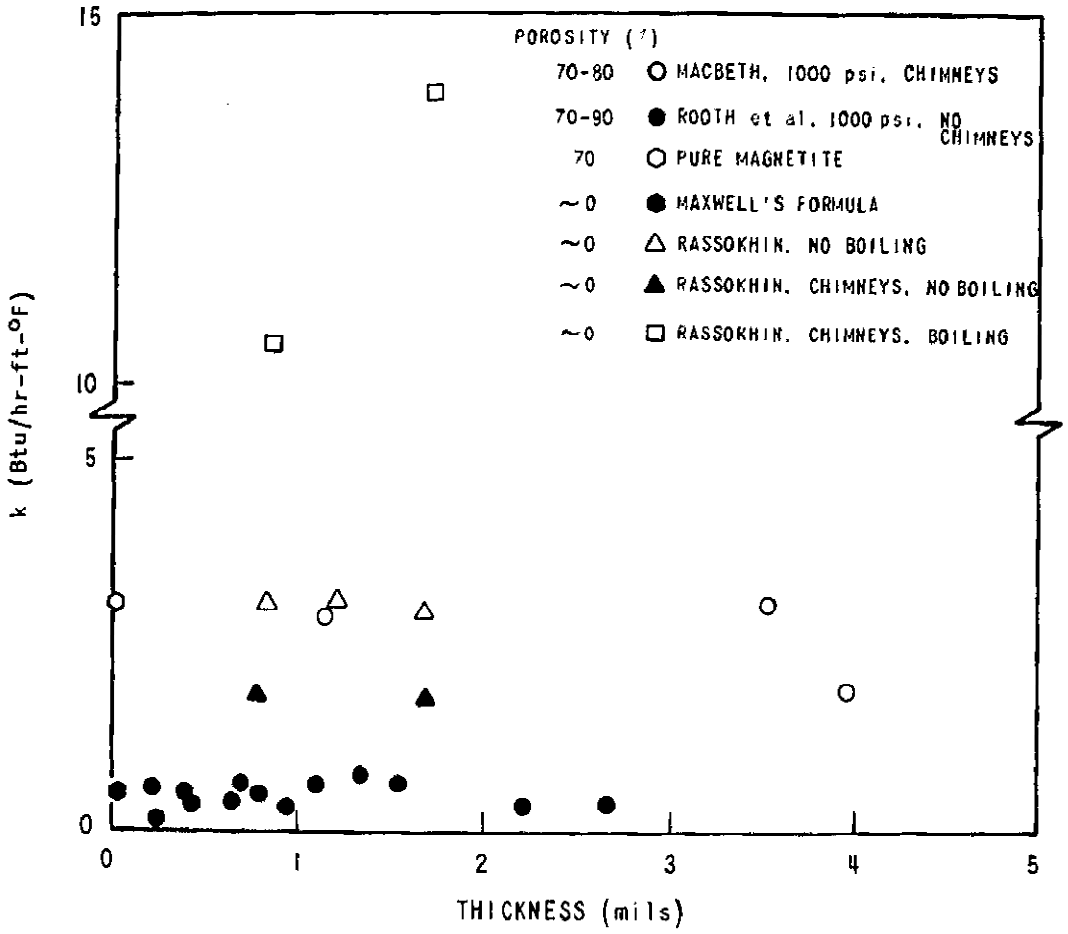

Figure 4.12: Effective Conductance of Magnetite Deposits

An analysis of the generation of vapor was completed. Figure 4.13 compares channel averaged vapor volume fraction for clean and crudded surfaces. Multiple items should be discussed here. First, vapor starts to generate (the two-phase region begins) between 600-700

kW/m^2. This agrees with the results in Figure 4.10. The crudded surface seems to generate a noticeable amount more of vapor once ~1200 kW/m^2 is reached. Referring to Figure 4.10, this is the heat flux where the results of the crudded surface crosses those for the clean surface. So, even though more vapor is generating on the crudded surface starting at this heat flux, it is also where heat transfer is enhanced. Overall, the crudded surface generates more vapor in the two-phase region (resulting from increased nucleation site density, decreased bubble diameter, and wick boiling present in the crud model), but does not always amount to degraded heat transfer. The reasons for this are discussed in Chapter 1.

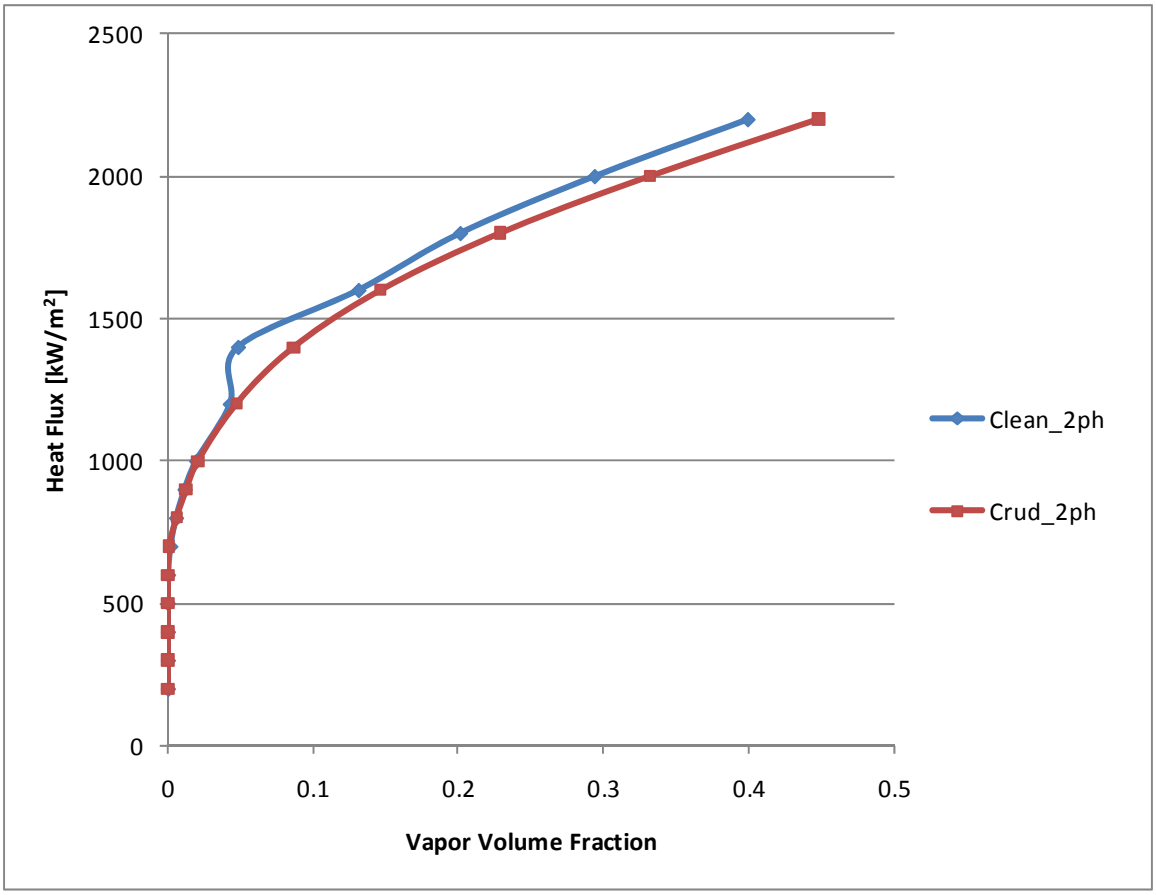

Figure 4.13: Difference in Vapor Volume Fraction Between Clean and Crudded Surfaces

Figure 4.13 shows that vapor volume fraction increases as the heat flux increases for clean and crudded surfaces. It can also be seen that more vapor is generated on a crudded surface than a clean surface at the same heat flux. Along with this discussion, Figure 4.14 and Figure 4.15 are predicted contour plots of vapor volume fraction. The volume fraction is highest along the heated surface at the end of the test section. Segments showing the last third of the test section in enlarged images are illustrated in Figure 4.16 and Figure 4.17. The generation of vapor is definitely greater on the crudded surface. Even though this is the case, maximum wall temperature at the outlet is greater for the clean surface ($T_{max}^{clean} = 451.6\ K\ and\ T_{max}^{crud} = 445.7\ K$). Again, this is due the enhanced heat transfer effects of crud at high heat fluxes resulting from wick boiling. (Contours of temperature are displayed for different heat fluxes of clean and crudded surfaces in Appendix A.)

Figure 4.14: Predicted Contours of Vapor Volume Fraction on Clean Surface (q'' = 2000 kW/m^2)

Figure 4.15: Predicted Contours of Vapor Volume Fraction on Crudded Surface (q'' = 2000 kW/m^2)

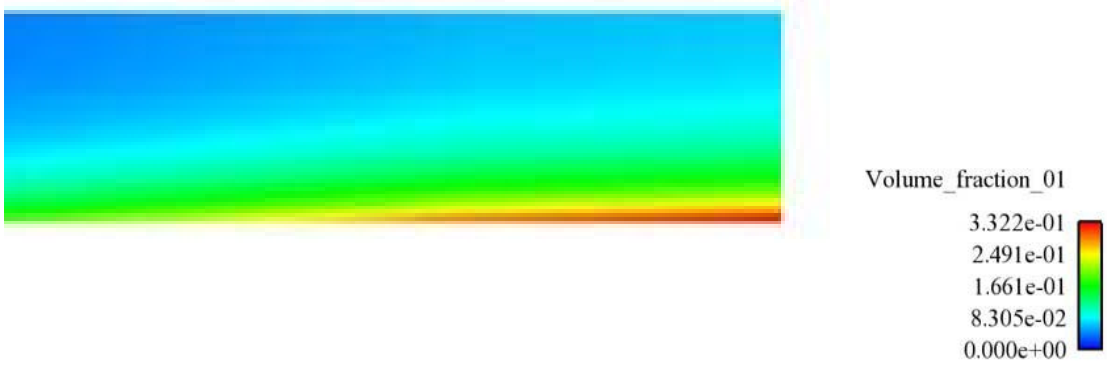

Figure 4.16: Predicted Contours of Vapor Volume Fraction on Clean Surface (q'' = 2000 kW/m^2) – Enlarged View

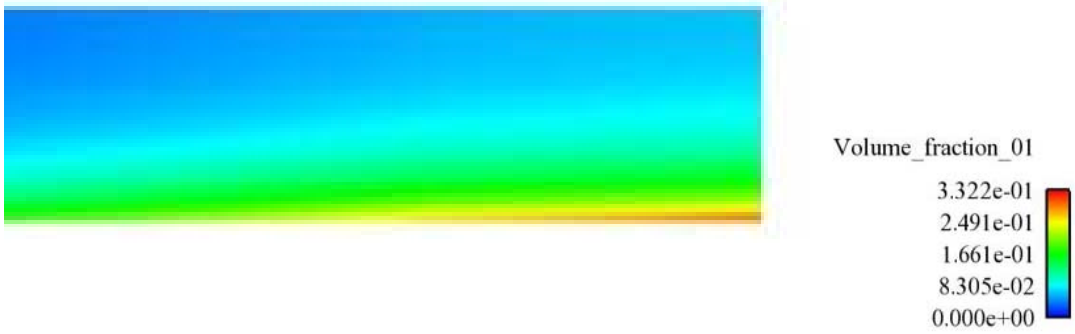

Figure 4.17: Predicted Contours of Vapor Volume Fraction on Crudded Surface (q'' = 2000 kW/m^2) – Enlarged View

In Figure 4.18 through Figure 4.20, contours of condensation mass transfer, Γ^{vl}, are shown. The behaviour of this model is quite interesting, being driven by both local subcooling and vapor (i.e., donor) mass fraction. As boiling begins to develop in the channel, virtually all of the vapor condenses because the subcooling (and, thereby, the condesnation rate) is high. The condensation rate reaches a maximum near the point where vigorous boiling begins (i.e. lots of donor phase is available) and significant subcooling also exists. Condensation is seen to diminish towards the exit of the channel, where the liquid approaches saturation. A similar effect is seen in the crudded case in Figure 4.19. Condensation mass transfer takes place where vapor is present. For a case with a lower heat flux (Figure 4.20), condensation mass transfer happens further down the test section since vapor is not generated until this axial location. From comparing Figure 4.18 and Figure 4.20, it is concluded that much less condensation mass transfer occurs at lower heat fluxes. This is because there is less vapor generated at lower heat fluxes resulting in less condensation mass transfer occuring altogether.

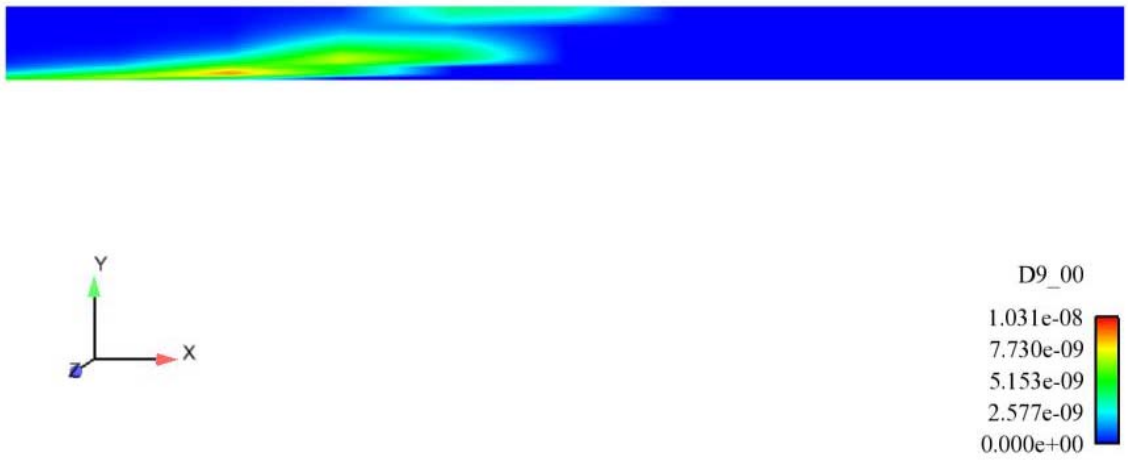

Figure 4.18: Predicted Contours of Condensation Mass Transfer of Liquid on Clean Surface (q'' = 2000 kW/m^2)

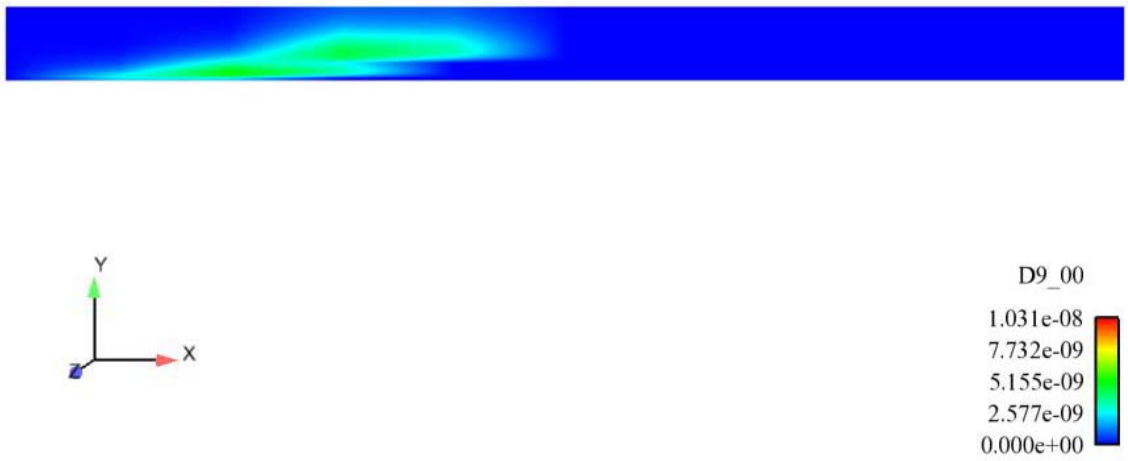

Figure 4.19: Predicted Contours of Condensation Mass Transfer of Liquid on Crudded Surface (q'' = 2000 kW/m^2)

Figure 4.20: Predicted Contours of Condensation Mass Transfer of Liquid on Clean Surface (q'' = 900 kW/m^2)

Chapter 5 Conclusions

Modeling of subcooled boiling in crudded nuclear reactor coolant passages of pressurized water reactors using CFD was the focus of this research. An Eulerian multiphase subcooled boiling model was implemented in a multidimensional CFD code to predict the heat transfer in vertical coolant passages with inlet subcooling, with and without crud deposits present on the heated surface. This model was based on a heat apportionment algorithm. It was demonstrated that the heat apportionment algorithm can accurately predict clean surface nucleate boiling for two validation cases. The first of these was Bartolomei which was selected for having prototypic conditions of a PWR along with experimental data including CFD calculations. The second was Cohen and Taylor data which is non-prototypic, but one of the only sets of crudded data available. The heat apportionment model predicted many thermal hydraulic parameters of interest accurately including bulk volume fraction. Qualitative distribution of vapor volume fraction and liquid temperature were presented to elucidate some of the physics present.

A model was developed for crudded boiling based on the heat apportionment approach. This model incorporated four physical elements of the deposits: surface roughness, crud layer conductivity, nucleation modification, and wick boiling. A dimensionally and physically consistent approach to modeling each of these was presented. It was observed that the proposed model can accurately predict the boiling heat transfer physics of a crudded surface. In particular, it was shown that the model can capture the point of heat transfer enhancement from the crud. This enhancement can be attributed to wick boiling becoming important enough that it overwhelms the insulating behavior of the crud. It is important to note that the wick boiling model was calibrated to match the Cohen and Taylor data, whereas the other model coefficients arose naturally from system parameters or experimental observation.

In the view of the author, it has been demonstrated that the heat apportionment crud boiling model as presented is a suitable framework for capturing all of the relevant physics in crudded subcooling nucleate boiling flows.

5.1 **Suggestions for Future Work**

Firstly, there remains an important need for more high pressure subcooled boiling data on heated surfaces with crud deposits present. Most importantly, under typical PWR operating conditions.

Secondly, several models in the baseline formulation are non-local. That is, are dependent on $T^w - T^{bulk}$, where T^{bulk} is a far field liquid temperature, and as such, are not well suited to multidimensional CFD. Models for nucleation site density and bubble diameter should be reformatted based on local rather than system parameters.

Thirdly, additional experimental data on crudded boiling could be used to refine the wick boiling crud model presented. In particular, the exponent on the wall superheat could be calibrated to a higher number in order to account for a likely super-linear increase in chimney jetting and, thereby, heat transfer coefficient, with clad superheat. Also, constant κ could be formulated using dimensional analysis to accommodate other system parameters that could be of importance in wick boiling.

Fourthly, development of more appropriate lift and repulsion models are identified as future work.

REFERENCES

1. **Podowski, Michael Z. and Podowski, Raf M.** *Mechanistic Multidimensional Modeling of Forced Convection Boiling Heat Transfer.* s.l. : Hindawi Publishing Corporation, 2008.

2. **Wang, Guoqiang.** *Improved Crud Heat Transfer Model for Dryout on Fuel Pin Surfaces at PWR Operating Conditions.* Department of Mechanical and Nuclear Engineering, The Pennsylvania State University. 2009. Dissertation.

3. **Tondreas, Neil E. and Kazimi, Mujid S.** *Nuclear Systems I: Thermal Hydraulic Fundamentals.* New York, NY : Taylor and Francis Group, 1990.

4. **Macbeth, R. V., Trenberth, R. and Wood, R. W.** *An Investigation into the Effect of "Crud" Deposits on Surface Temperature, Dry-out and Pressure Drop, with Forced Convection Boiling of Water at 69 Bar in an Annular Test Section* . Winfrith : s.n., 1971. AEEW-R-705.

5. *Heat and Mass Transfer for Boiling in Porous Deposits with Chimneys.* **Cohen, Paul.** No. 138, 1974, AICHe Symposium Series, Vol. 70, pp. 71-80.

6. *Boiling Heat Transfer Data at Low Heat Flux.* **Elrod, W. C., et al.** 1967, Journal of Heat Transfer.

7. *Concentration Level of Solutes in Porous Deposits with Chimneys under Wick Boiling Conditions.* **Pan, C., Jones, B. G. and Machiels, A. J.** 1987, Nuclear Engineering and Design, Vol. 99, pp. 317-327.

8. *On the Modeling of Multidimensional Effects in Boiling Channels.* **Kurul, Necdet and Podowski, Michael Z.** Minneapolis, MN : s.n., 1991, ANS Proceedings of the 27th National Heat Transfer Conference.

9. *CFD Modelling of Subcooled Boiling- Concept, Validation and Application to Fuel Assembly Design.* **Krepper, Eckhard, Koncar, Bostjan and Egorov, Yury.** 2007, Nuclear Engineering and Design, Vol. 237, pp. 716-731.

10. *Experimental Implementation of the RPI Wall Boiling Model in CFX-5.6.* **Egorov, Y. and Menter, F.** ANSYS Germany GmbH : s.n., 2004. Technical Report ANSYS/TR-04-10.

11. *Vapor Bubble GRowth Rate and HEat Transfer Intensity at Subcooled Water Boiling.* **Tolubinsky, V. I. and Kostanchuk, D. M.** 1970, Preprints of papers presented at the 4th Internaional HEat tRansfer Conference, Vol. 5. Paper No. B-2.8.

12. *Computational Analysis of a Subcooling Boiling Flow with a One-Group Interfacial Area Transport Equation.* **Bae, Byong-Uhn, et al.** 4, 2008, Journal of Nuclear Science and Technology, Vol. 45, pp. 341-351.

13. *Modeling of Subcooled Nucleate boiling in a Vertical Channel with Coupling of Bubble-Tracking and Two-Fluid Models.* **Kljenak, Ivo, Koncar, Bostjan and Mavko, Borut.** Stockholm, Sweden : s.n., October 10-11, 2006, Workshop on Modeling and Measurements of Two-Phase Flow and Heat Transfer in Nuclear Fuel Assemblies.

14. *A Wall Heat Transfer Model for Subcooled Boiling Flow.* **Steiner, Helfriend, Kobor, Alexander and Gebhard, Ludwig.** 2005, Int. Journal of Heat and Mass Transfer, Vol. 48, pp. 4163-4173.

15. *A Correlation for Boiling Heat Transfer to Saturated Fluids in Convective Flow.* **Chen, J. C.** Boston : s.n., 1963. ASME preprint 63 HT34 presented at the 6th National Heat Transfer Conference.

16. *An Experimental Investigation of True Volumatric Vapour Content with Subcooled Boiling in Tubes.* **Bartolomei, G. G., et al.** 1982, Thermal Engineering, Vol. 29, pp. 132-135.

17. *Experimental Study of True Void Fraction when Boiling Subcooled Water in Vertical Tubes.* **Bartolemei, G. G. and Chanturiya, V. M.** 2, 1967, Tepleonergetika, Vol. 14, pp. 80-83.

18. *Validation of Two-Fluid Eulerian CFD Modeling for Microbubble Drag Reduction Accross a Wide Range of Reynolds Numbers.* **Kunz, R. F., et al.** 2007, ASME Journal of Fluids Engineering, Vol. 129, pp. 66-79.

19. *Phase Distribution in Bubbly Two-Phase Flow in Vertical Ducts.* **DeBertadano, M. L., Lahey, R. T. Jr. and Jones, O. T.** 5, International Journal of Multi-phase Flow, Vol. 20, p. 805.

20. *Deformable Bubbles in a Free Shear layer.* **Loth, E., Taeibi-Rahni, M. and Tryggvason, G.** 5, September 1997, International Journal of Multiphase Flow, Vol. 23, pp. 997-1001.

21. *Analysis of Phase Distribution in Fully Developed Laminar Bubbly Two-Phase Flow.* **Antal, S. P., Lahey, R. T. Jr. and Flaherty, J. E.** 5, 1991, International Journal of Two-Phase Flow, Vol. 17, pp. 635-652.

22. *Numerical Modeling of Bubble Distributions in Horizontal Bubbly Channel Flow.* **Kawamura, T. and Yoshiba, H.** Yokohama, Japan : s.n., 2004. Proceedings of the 5th Int. Conf. on Multiphase Flow. Paper No. 354.

23. **Schlichting, Hermann.** *Boundary-Layer Theory.* 1979.

24. **White, Frank M.** *Viscous Fluid Flow.* 1974.

25. *Enhancements of the SIMPLE Method for Predicting Incompressible Fluid Flows.* **Van Doormal, J. P. and Raithby, G. D.** 1984, Numerical Heat Transfer, Vol. 7, pp. 147-163.

26. *Numerical Study of the Turbulent Flow Past an Airfoil with Trailing Edge Separation.* **Rhie, C. M. and Chow, W. L.** 1983, AIAA Journal, Vol. 21, p. 1527.

27. *A Couple Phasic Exchange Algorithm for Multi-Dimensional Four-Field Analysis of Heated Flows with Mass Transfer.* **Kunz, R. F., et al.** 7, 1998, Computers and Fluids, Vol. 27.

28. *A Pressure-Based Unstructured Grid Method for All-Speed Flows.* **Lien, F. S.** 2000, International Journal of Numerical Methods in Fluids, Vol. 33.

29. *Imterpetation of Pressure-Based Methods as Time Marching Schemes.* **Venkateswaran, S., Tamamidis, P. and Merkle, C. L.** s.l. : Singer Lecture Notes in Physics. Proceedings 15th International Conference on Numerical Methods in Fluid Dynamics.

30. *Three-Dimensional Numerical Modeling of Phase Distribution of Two-Fluid Flow in Elbows and Return Beads.* **Carver, M. B. and Salcudean, M.** 1986, Numerical Heat Transfer, Vol. 10, pp. 229-251.

31. *Numerical Prediction of Phase Separation in Two-Phase Flow Through T-Junctions.* **Issa, R. I. and Oliviera, P. J.** 2, 1994, Computers and Fluids, Vol. 23, pp. 347-372.

32. *Mathematical Methods in Nuclear-Reactor Thermal Hydraulics.* **Spalding, D. B.** Saratoga, NY : s.n., 1980. Keynote Paper, ANS Meeting on Nuclear-Reactor Thermal Hydraulics.

33. PETSc. [Online] [Cited: 4 15, 2010.] http://www.mcs.anl.gov/petsc/petsc-as/.

34. *On the Roles of Realizability, Boundary Conditions and Artificial Dissipation in Two-Fluid Simulations with Interfacial Forces.* **Kunz, R. F.** Aussois, France : s.n., 2000. presented AMIF-ESF Conference on Computing Methods in Two-Phase Flow.

35. **Kunz, Robert F., et al.** *An Unstructured Two-Fluid Method Based on the Coupled Phasic Exchange Algoritm.* s.l. : American Institute of Aeronautics and Astronautics, 2001. AIAA-2001-2672.

36. **Tables, ASME Steam.** www.steamtablesonline.com. *Based on the industrial formulation for calculation of properties of water and steam, called:"IAPWS Industrial Formulation 1997 for the Thermodynamic Properties of Water and Steam (IAPWS-IF97)".* [Online]

37. **Hochreiter, Lawrence.** *Class Notes for Nuclear Engineering 430, Thermal Hydraulics.* 2008. pp. 2-77. Penn State University.

38. **Tong, L. S. and Tang, Y. S.** *Boiling Heat Transfer and Two-Phase Flow, 2nd Edition.* Washington D.C. : Taylor & Francis, 1997.

39. **Lamarsh, John R. and Baratta, Anthony J.** *Introduction to Nuclear Engineering, 3rd Edition.* Upper Saddle River, NJ : Prentice Hall, 2001.

40. *Convective Subcooled Boiling - Application Briefs from Fluent.* s.l. : Fluent Inc., 2004. EX222.

41. *Linear and Non-linear Iterative Methods for the Incompressible Navier-Stokes Equations.* **Clift, S. S. and Forsyth, P. A.** 1994, International Journal for Numerical Methods in Fluids, Vol. 18, pp. 229-256.

42. *An Analysis of Two-Phase Flow and Heat Transfer Using a Multidimensional, Multi-field, Two-Fluid Computational Fluid Dynamics (CFD) Model.* **Lahey, R. T. and Drew, D. A.** Santa Barbara, California : s.n., 2000. Japan/US Seminar of Two-Phase Flow Dynamics.

43. *Development of a Next Genertion Computer Code for the Prediction of Multicomponent Multiphase Flows.* **Antal, S. P., et al.** Cargese, France : s.n., 2000. International Meeting on Trends in Numerical and Physical Modeling for Industrial Multiphase Flow.

APPENDIX A

This appendix includes individual cases run in NPHASE-PSU including single phase and two-phase cases on clean and crudded surfaces. The results of eliminating the wick boiling model are also included. Contours of liquid temperature are displayed clean and crudded surfaces at different heat fluxes.

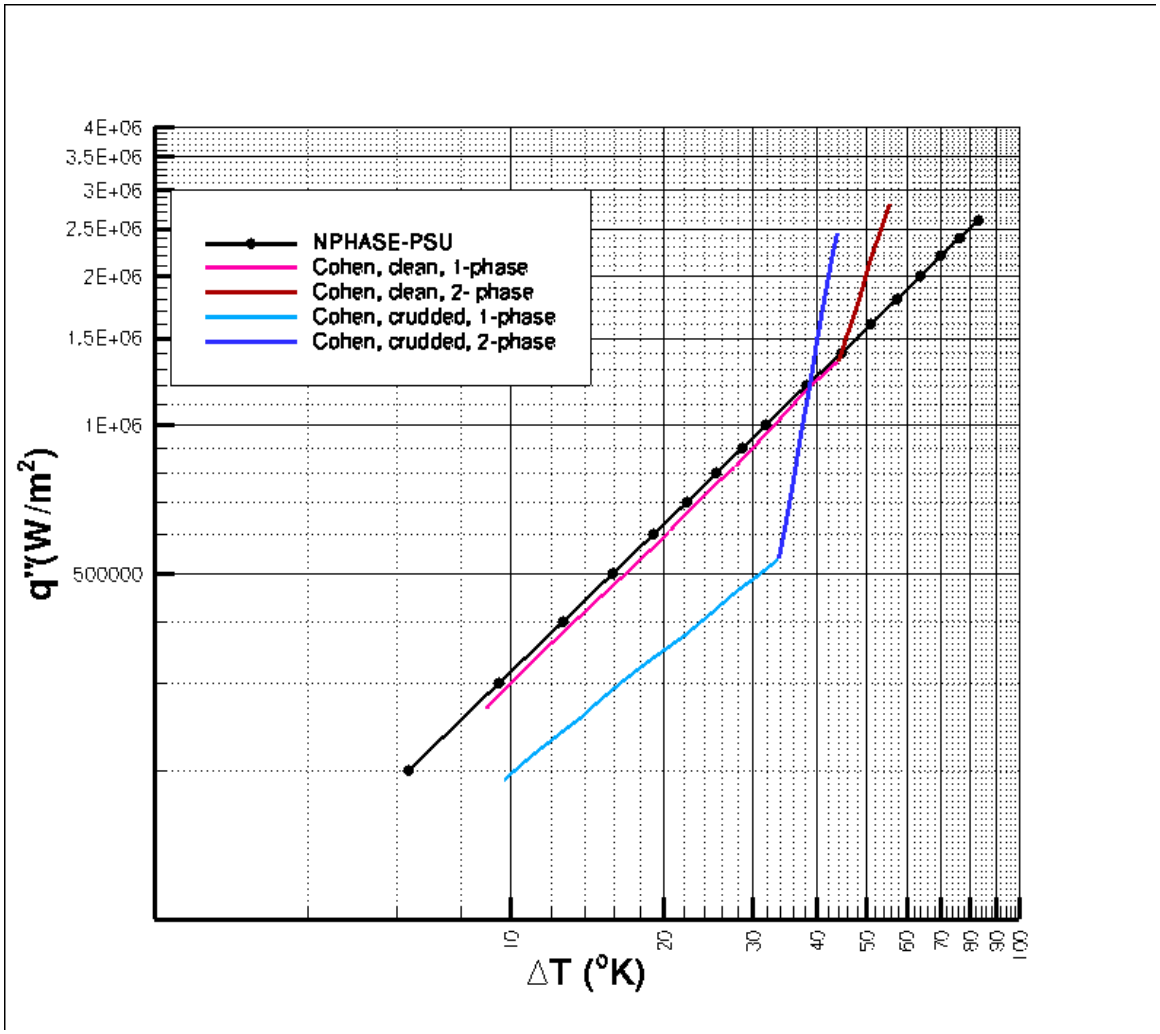

Figure 0.1: Comparison of Single Phase Results for Clean Surface

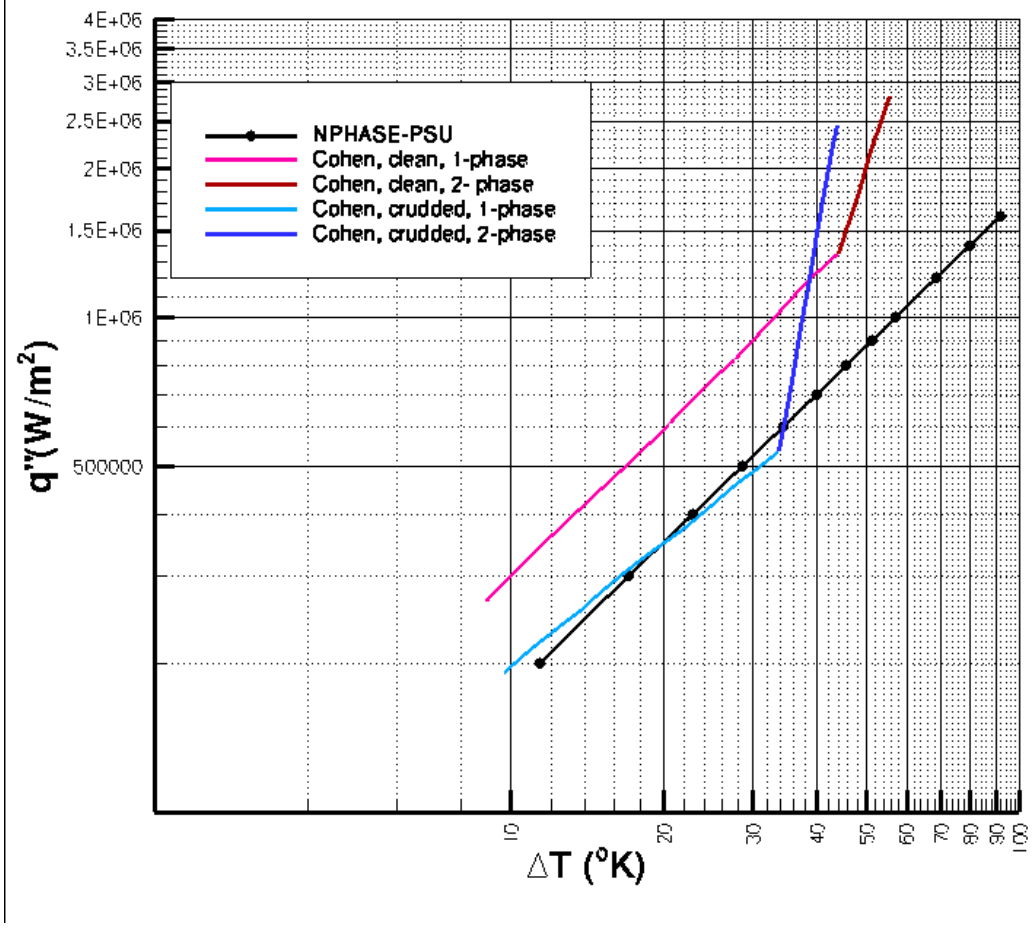

Figure 0.2: Comparison of Single Phase Results for Crudded Surface

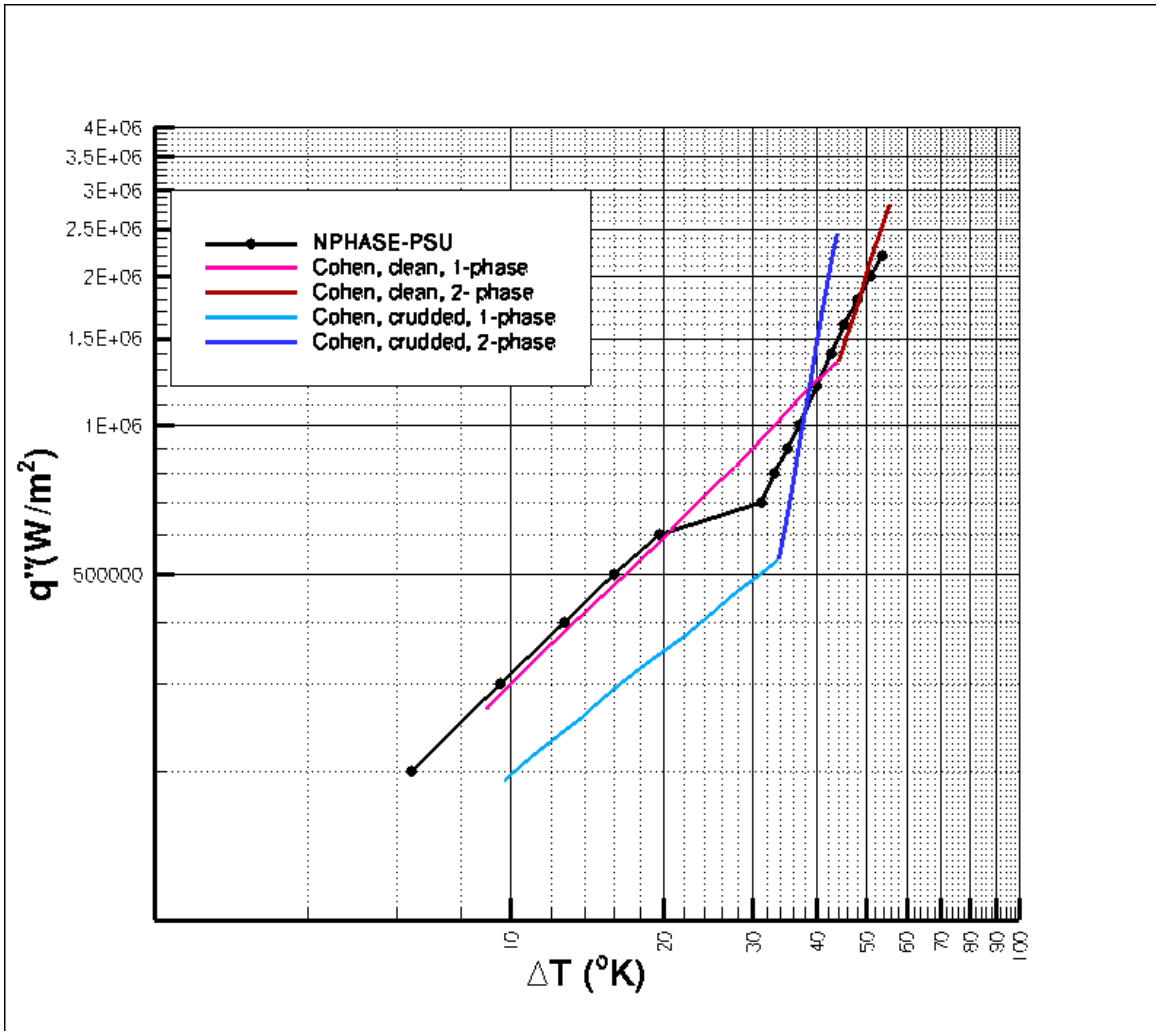

Figure 0.3: Comparison of Two-Phase Results for Clean Surface

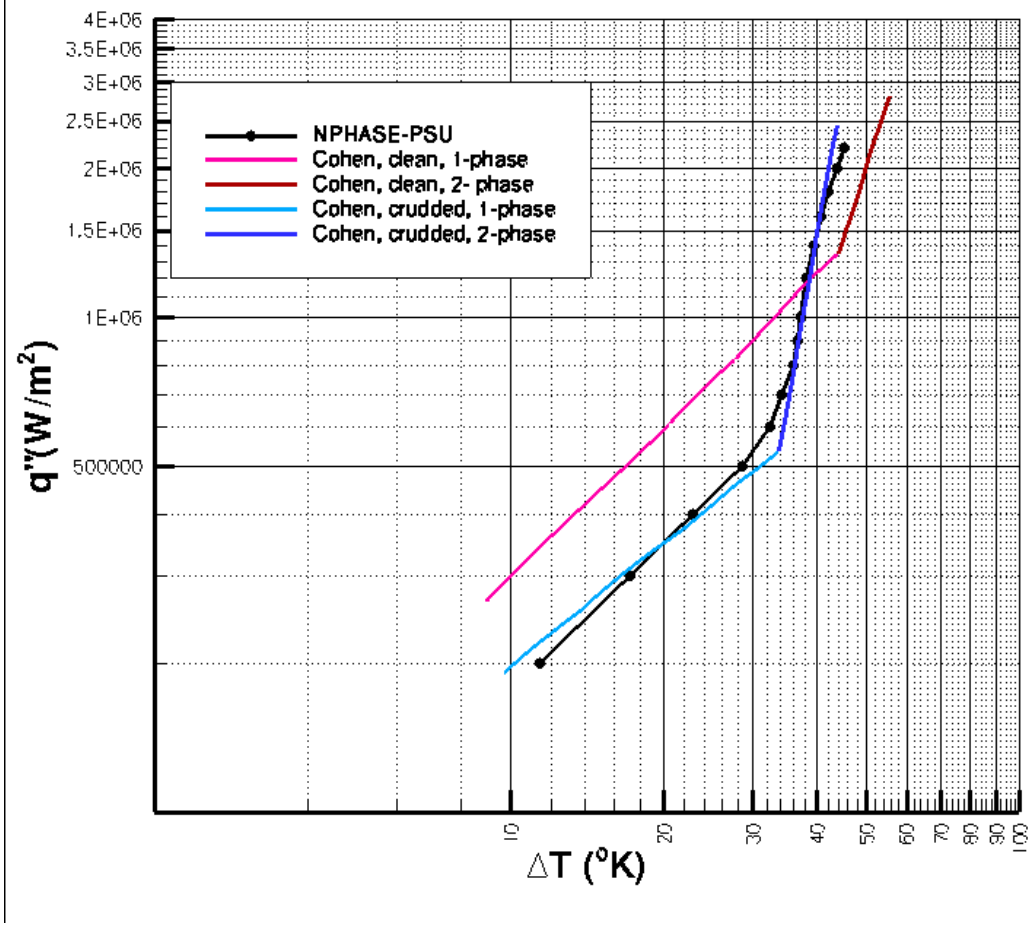

Figure 0.4: Comparison of Two-Phase Results for Crudded Surface

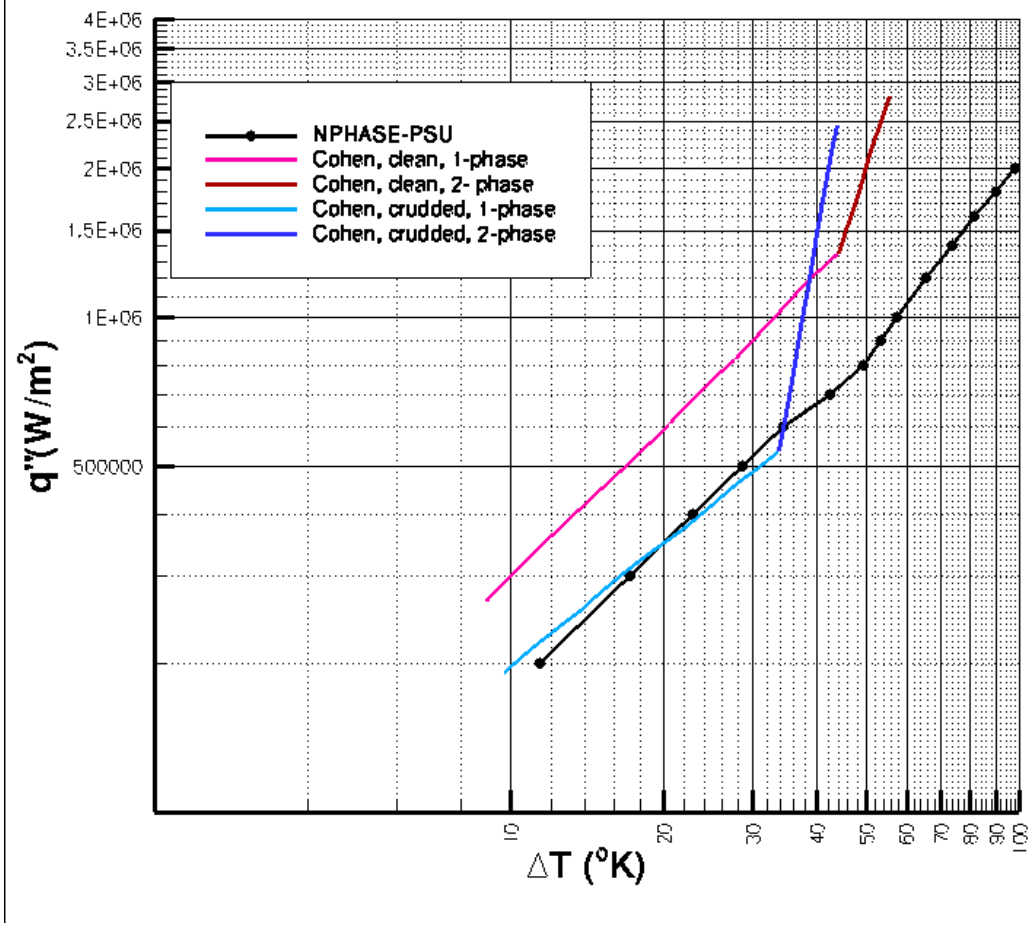

Figure 0.5: Two-Phase Results with Wick Boiling for Crudded Surface

Figure 0.6: Predicted Contours of Liquid Temperature on Clean Surface (q'' = 2000 kW/m^2)

Figure 0.7: Predicted Contours of Liquid Temperature on Crudded Surface (q'' = 2000 kW/m^2)

Figure 0.8: Predicted Contours of Liquid Temperature on Clean Surface (q'' = 900 kW/m^2)

Figure 0.9: Predicted Contours of Liquid Temperature on Clean Surface (q'' = 900 kW/m^2)